UCLA
UCLA Previously Published Works

Title

Regulation of Oxygenic Photosynthesis during Trophic Transitions in the Green Alga Chromochloris zofingiensis [OPEN]

Permalink

https://escholarship.org/uc/item/2js8161p

Journal

The Plant Cell, 31(3)

ISSN

1040-4651

Authors

Roth, Melissa S
Gallaher, Sean D
Westcott, Daniel J
et al.

Publication Date

2019-03-01

DOI

10.1105/tpc.18.00742

Peer reviewed

Check for updates

LARGE-SCALE BIOLOGY ARTICLE

Regulation of Oxygenic Photosynthesis during Trophic Transitions in the Green Alga *Chromochloris zofingiensis*[OPEN]

Melissa S. Roth,[a,b,1] Sean D. Gallaher,[c] Daniel J. Westcott,[a,b] Masakazu Iwai,[a,b] Katherine B. Louie,[d,e] Maria Mueller,[b,f] Andreas Walter,[g,h] Fatima Foflonker,[i] Benjamin P. Bowen,[d,e] Nassim N. Ataii,[b] Junha Song,[b] Jian-Hua Chen,[g,h] Crysten E. Blaby-Haas,[i] Carolyn Larabell,[g,h] Manfred Auer,[b,f] Trent R. Northen,[d,e] Sabeeha S. Merchant,[c,2] and Krishna K. Niyogi[a,b,1]

[a] Howard Hughes Medical Institute, Department of Plant and Microbial Biology, University of California, Berkeley, California 94720-3102
[b] Molecular Biophysics and Integrated Bioimaging Division, Lawrence Berkeley National Laboratory, Berkeley, California 94720
[c] Department of Chemistry and Biochemistry and Institute for Genomics and Proteomics, University of California, Los Angeles, California 90095-1569
[d] Environmental Genomics and Systems Biology Division, Lawrence Berkeley National Laboratory, Berkeley, California 94720
[e] U.S. Department of Energy Joint Genome Institute, Walnut Creek, California 94598
[f] Joint BioEnergy Institute, Lawrence Berkeley National Laboratory, Berkeley, California 94720
[g] Department of Anatomy, University of California, San Francisco, California 94143
[h] National Center for X-ray Tomography, Lawrence Berkeley National Laboratory, Berkeley, California 94720
[i] Biology Department, Brookhaven National Laboratory, Upton, New York 11973

ORCID IDs: 0000-0001-7389-5982 (M.S.R.); 0000-0002-9773-6051 (S.D.G.); 0000-0002-1828-2582 (D.J.W.); 0000-0002-0986-9015 (M.I.); 0000-0002-6787-7558 (K.B.L.); 0000-0003-0451-5442 (M.M.); 0000-0002-4096-1944 (A.W.); 0000-0002-0472-8192 (F.F.); 0000-0003-1368-3958 (B.P.B.); 0000-0002-8033-8700 (N.N.A.); 0000-0003-2015-1749 (J.S.); 0000-0002-7998-0878 (J.-H.C.); 0000-0002-1583-1291 (C.E.B.-H.); 0000-0002-6262-4789 (C.L.); 0000-0002-5435-9436 (M.A.); 0000-0001-8404-3259 (T.R.N.); 0000-0002-2594-509X (S.S.M.); 0000-0001-7229-2071 (K.K.N.)

Light and nutrients are critical regulators of photosynthesis and metabolism in plants and algae. Many algae have the metabolic flexibility to grow photoautotrophically, heterotrophically, or mixotrophically. Here, we describe reversible Glc-dependent repression/activation of oxygenic photosynthesis in the unicellular green alga *Chromochloris zofingiensis.* We observed rapid and reversible changes in photosynthesis, in the photosynthetic apparatus, in thylakoid ultrastructure, and in energy stores including lipids and starch. Following Glc addition in the light, *C. zofingiensis* shuts off photosynthesis within days and accumulates large amounts of commercially relevant bioproducts, including triacylglycerols and the high-value nutraceutical ketocarotenoid astaxanthin, while increasing culture biomass. RNA sequencing reveals reversible changes in the transcriptome that form the basis of this metabolic regulation. Functional enrichment analyses show that Glc represses photosynthetic pathways while ketocarotenoid biosynthesis and heterotrophic carbon metabolism are upregulated. Because sugars play fundamental regulatory roles in gene expression, physiology, metabolism, and growth in both plants and animals, we have developed a simple algal model system to investigate conserved eukaryotic sugar responses as well as mechanisms of thylakoid breakdown and biogenesis in chloroplasts. Understanding regulation of photosynthesis and metabolism in algae could enable bioengineering to reroute metabolism toward beneficial bioproducts for energy, food, pharmaceuticals, and human health.

INTRODUCTION

Regulation of oxygenic photosynthesis and primary carbon metabolism in algae and plants is critical for net primary production of biomass on a global scale. Algae can regulate photosynthesis and

metabolism in response to changes in light and nutrient availability. Many algae have flexible metabolism and can change from photoautotrophic to mixotrophic and/or heterotrophic growth. The popular model green alga *Chlamydomonas reinhardtii* (Chlorophyceae) grows autotrophically in the light and either mixotrophically with the carbon source acetate in the light or heterotrophically with acetate in the dark (Harris, 2009). *C. reinhardtii* remains green in the presence of acetate in both light and dark, and even dark-grown cells remain capable of carbon fixation via photosynthesis in the light (Merchant et al., 2007). The green alga *Auxenochlorella protothecoides* (Trebouxiophyceae), formerly known as *Chlorella protothecoides* (Huss et al., 1999), changes its pigmentation from green to yellow to colorless depending on the amount of nutrients and carbon source (Shihira and

IN A NUTSHELL

Background: Photosynthesis is the life-sustaining process that plants and algae use to convert sunlight into the chemical energy that fuels the biosphere. It also produces the oxygen and sugars that we humans and other animals depend on. By understanding the factors that control photosynthesis, we can improve agriculture and the production of bioproducts and biofuels by both algae and plants. Algae control photosynthesis and metabolism in response to changes in light and nutrient availability. Glucose, an abundant and preferred carbon source for many organisms, regulates gene expression, metabolism, growth and aging in plants, animals, yeast and bacteria, but its regulatory role in algae is not well understood. We used the unicellular green alga *Chromochloris zofingiensis* that, unlike the closely related model green alga *Chlamydomonas reinhardtii*, is able to turn photosynthesis off and on in response to glucose. *Chromochloris* has recently become an alga of high commercial interest because it can produce both high amounts of lipids for biofuels and the high-value antioxidant, astaxanthin.

Question: We wanted to characterize the physiological, photosynthetic and metabolic changes during the glucose-induced repression and activation of photosynthesis. What are the underlying changes in gene expression controlling this photosynthetic switch in *Chromochloris*?

Findings: After just a few days of adding glucose in the light, *Chromochloris* represses photosynthesis, and the photosynthetic apparatus and membranes decrease. At the same time, cells accumulate biofuel precursors such as lipids and starch and the high-value antioxidant astaxanthin. Within a single day of removing glucose, photosynthesis resumes, and the photosynthetic apparatus reforms. Nearly 1/3 of all genes in the genome are affected by adding and removing glucose. Regulation of these genes is coordinated, reversible, and involves specific changes including repression of photosynthetic pathways and upregulation of lipid and carotenoid (e.g. astaxanthin) biosynthesis.

Next steps: Our work introduces an algal system with a readily controllable photosynthetic and metabolic switch that provides fundamental insights into photosynthesis and algal biology. Our future work aims to increase the amount of lipids and astaxanthin produced by *Chromochloris* to improve its commercial prospects for sustainable fuel and other valuable products.

Krauss, 1963). *A. prototheacoides* exhibits a dramatic degeneration of its chloroplast when grown with Glc, a phenomenon known as Glc-induced bleaching (Shihira-Ishikawa and Hase, 1964). More recently it was shown that Glc upregulates fatty acid (FA) synthesis genes and causes an accumulation of lipid droplets in *A. prototheacoides* (Gao et al., 2014). Insight into the molecular mechanisms that allow algae to increase biomass and accumulate high levels of lipids and starch when consuming exogenous reduced carbon will expand our knowledge of algal metabolism and improve the economic potential of algal biofuels and other bioproducts.

Sugars are critical metabolic and regulatory molecules in plants. Exogenous Glc, a preferred carbon source for many organisms, has been shown to repress photosynthesis while modulating plant growth and development (reviewed in Rolland et al., 2006; Sheen, 2014). Despite the early work on Glc-induced bleaching (Shihira and Krauss, 1963; Shihira-Ishikawa and Hase, 1964; Matsuka et al., 1969), a detailed understanding of Glc responses in green algae is presently lacking. There is renewed interest in improving algal biomass for both biofuels and bioproducts, and regulation and manipulation of algal growth under heterotrophic and mixotrophic conditions has become an active area of investigation.

Chromochloris zofingiensis (Chlorophyceae) is emerging as a model for investigating metabolic flexibility in green algae because it can be cultivated in multiple trophic modes (Chen et al., 2015b; Zhang et al., 2017) on a variety of carbon sources (Sun et al., 2008) and has a high-quality chromosome-level small (~58-Mbp) genome and transcriptome (Roth et al., 2017). Also, research on *C. zofingiensis* can benefit from its similarity to *C. reinhardtii*, a closely related alga that has been widely studied in terms of its biology, genetics, and biochemistry. *C. zofingiensis*, which was placed in *Chlorella*, *Muriella*, and *Mychonastes* before its

current placement into *Chromochloris* (Fucikova and Lewis, 2012), is an ~4-μm unicellular, haploid, coccoid alga with a mitochondrial network and a single starch-containing chloroplast (Roth et al., 2017). In contrast to *C. reinhardtii*, *C. zofingiensis* can grow with Glc as its sole carbon source, and has an expanded number of hexose transporter genes, suggesting the ability to acclimate to a wide variety of environmental conditions (Suzuki et al., 2018). Under specific conditions such as heterotrophy, nitrogen deprivation, or high light, *C. zofingiensis* accumulates high amounts of the valuable secondary ketocarotenoid astaxanthin and biofuel precursors (Breuer et al., 2012; Liu et al., 2014; Mulders et al., 2014; Huang et al., 2016; Zhang et al., 2016; Roth et al., 2017). Astaxanthin has a variety of commercial applications such as in feed and cosmetics, and recent studies have highlighted its value as a pharmaceutical. Naturally produced astaxanthin is a potent antioxidant and anti-inflammatory agent that can improve human health and combat disease (Hussein et al., 2006; Yuan et al., 2011; Liu et al., 2014). *C. zofingiensis* has been recently recognized as one of the highest producers of the biofuel precursor triacylglycerol (TAG) (Breuer et al., 2012). This combination of valuable attributes has led to increased biological and commercial interest in *C. zofingiensis*.

Using cellular physiology analyses, transcriptomics, lipid analyses, transmission electron microscopy (TEM), soft x-ray tomography (SXT), and structured illumination microscopy (SIM), we provide insight into Glc-dependent repression and activation of oxygenic photosynthesis that occurs in *C. zofingiensis* during trophic transitions. Within a few days of Glc addition in the light, photosynthetic efficiency declines to zero, and oxygen evolution in the light ceases. There is a loss of the photosynthetic apparatus, and thylakoid ultrastructure changes dramatically as membranes become reduced and overall
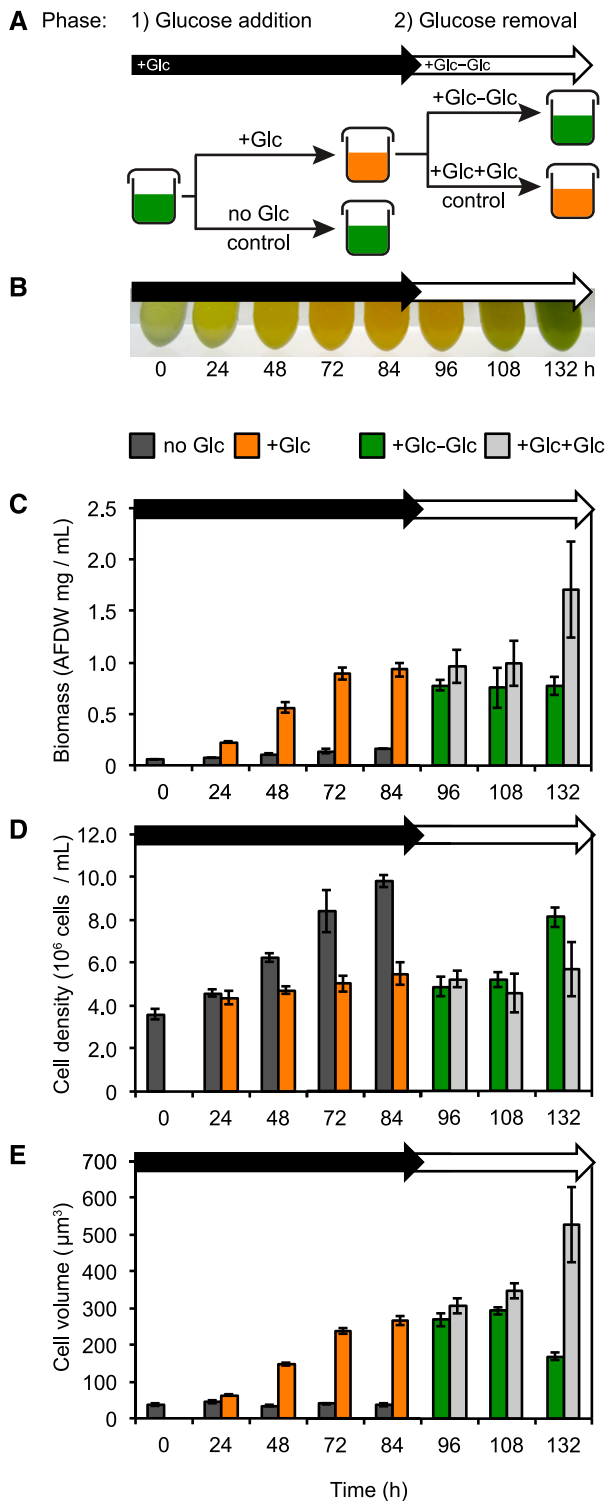
Figure 1. Overview of Glc Addition and Removal Experiment.

(A) Schematic of the experimental design, showing the Glc addition (black arrows) and Glc removal (white arrows) phases (see "Methods"). The first phase of the experiment (0 to 84 h) involves Glc addition (+Glc, orange), with photoautotrophic controls with no Glc added (no Glc, dark gray). In the second phase of the experiment (84 to 132 h), heterotrophic cells

thylakoid volume decreases. We observed an increase in energy stores, including starch and lipids and in particular TAGs. These changes were reversed upon removal of Glc within 2 d. Genome-wide analyses over a 12-h time course of Glc addition and removal revealed broad, reversible transcriptomic changes involving a third of all gene models. Glc represses photosynthetic pathways and upregulates ketocarotenoid and FA biosynthesis and modification. Our work highlights the utility of *C. zofingiensis* as a simple emerging model system to investigate the regulation of photosynthesis, thylakoid membrane dynamics, sugar responses, and changing metabolic modes in the green lineage.

RESULTS

Two-Phase Glc Addition and Glc Removal Experiment

To assess the effects of Glc on photosynthesis in *C. zofingiensis*, we conducted a two-phase experiment of Glc addition and subsequent removal in the light (Figure 1A). In the first phase (0 to 84 h), we added Glc to photoautotrophic cultures and maintained parallel cultures without Glc as photoautotrophic controls (see "Methods"). In the second phase (84 to 132 h), we removed Glc from heterotrophic cultures and provided fresh media without Glc. Additionally, we maintained parallel cultures where we removed Glc and provided fresh media with Glc as heterotrophic controls. Cultures were maintained in diurnal light (at 100 μmol photons m^{-2} s^{-1}) on a 16-h-light/8-h-dark cycle. Green cells turned orange in the presence of Glc due to an increase in ketocarotenoids, and these cells reverted to green after Glc removal (Figure 1B). Because previous studies have characterized Glc induction of ketocarotenoid biosynthesis and, in particular, astaxanthin accumulation in *C. zofingiensis* in both the light and dark (Ip et al., 2004; Ip and Chen, 2005; Li et al., 2008; Sun et al., 2008), we focused here on Glc-induced changes in photosynthesis, metabolism, and energy stores in the light. Whereas culture biomass and cell size increased with Glc, cell density in cultures increased more slowly with Glc, suggesting a decrease in the rate of cell division during the 0- to 84-h time course of our experiment (Figures 1C to 1E). Physiological, lipid, transcriptomic, and structural changes were analyzed during both Glc addition and Glc removal phases.

Glc Causes a Reversible Decline in Photosynthesis and the Photosynthetic Machinery

Glc caused a rapid decline in photosynthetic activity that recovered after Glc was removed. The maximum efficiency of PSII (F_v/F_m) decreased from 0.66 $\pm$ 0.01 to 0.01 $\pm$ 0.01 with Glc within

(+Glc) are pelleted and resuspended in fresh medium without Glc (+Glc–Glc, green). Heterotrophic controls (no Glc removal) are pelleted and resuspended in fresh medium containing Glc (+Glc+Glc, light gray).
(B) Representative concentrated *C. zofingiensis* cultures during the Glc addition/removal experiment.
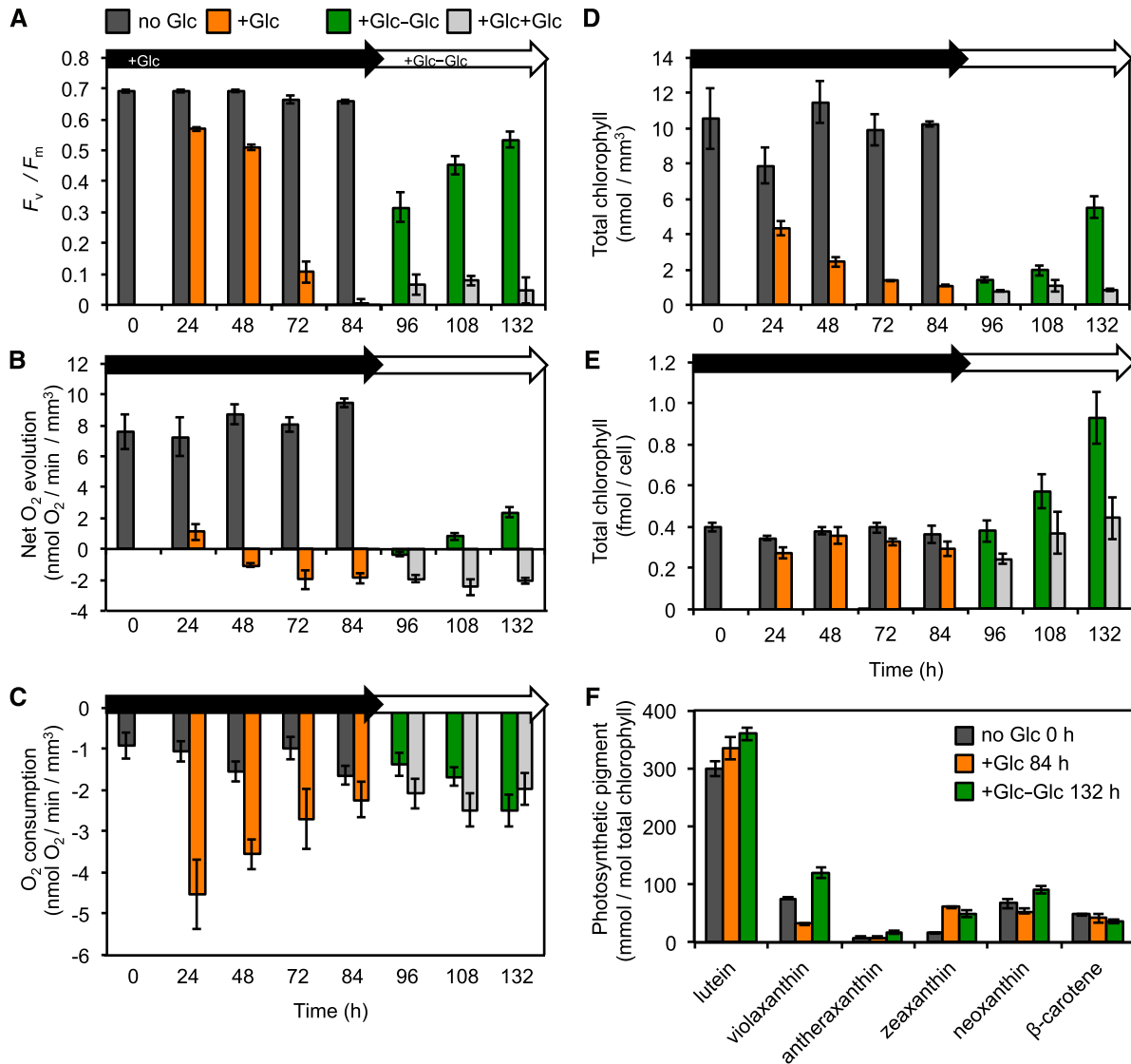**(C)** Culture biomass (AFDW) dynamics during Glc addition and removal.
(D) Cell density dynamics during Glc addition and removal.
(E) Individual cell volume dynamics during Glc addition and removal. The following color scheme is used for **(C)** to **(E)**: no Glc, dark gray; +Glc, orange; +Glc-Glc, green; +Glc+Glc, light gray. Data for **(C)** to **(E)** represent means $\pm$ sd (n = 3 to 4 biological replicates).

84 h (Figure 2A) and recovered after Glc removal. Furthermore, net oxygen evolution (production in the light) decreased from 9.4 ± 0.3 to -1.9 ± 0.4 nmol O_2 min^{-1} mm^{-3} with Glc (Figure 2B, results normalized to cell volume). Within 48 h, oxygen consumption in heterotrophic cultures surpassed oxygen production in the light.

The changes in net oxygen evolution were reversed after Glc removal. There was a decrease in chlorophyll per unit cell volume (Figure 2D), and there was also a loss of net oxygen evolution per unit of chlorophyll (Supplemental Figure 1A). These data suggest that residual chlorophyll is not associated with functional reaction

Figure 2. Glc Causes Reversible Repression of Photosynthesis.

(A) Maximum photosynthetic efficiency (F_v/F_m) dynamics during Glc addition and removal.

(B) Dynamics of net oxygen evolution (oxygen production in the light, at 100 μmol photons m^{-2} s^{-1}) during Glc addition and removal (data normalized to cell volume). See Supplemental Figure 1 for data normalized to chlorophyll.

(C) Dynamics of oxygen consumption in the dark during glucose addition and removal. See Supplemental Figure 1 for data normalized to chlorophyll.

(D) Total chlorophyll (chlorophylls a and b) dynamics during glucose addition and removal normalized by cell volume. See Supplemental Figure 1D for HPLC chromatograms.

(E) Total chlorophyll (chlorophylls a and b) dynamics during glucose addition and removal normalized per cell. Data were tested for significance ($P < 0.05$) using two-tailed t-test in JMP (v8.0). See Supplemental Figure 1D for HPLC chromatograms.

(F) Photosynthetic pigments relative to total chlorophyll during Glc addition and removal. Data were tested for significance ($P < 0.05$) using two-tailed t test in JMP (v8.0). See Supplemental Figure 1D for HPLC chromatograms.

The following color scheme is used for **(A)** to **(F)**: no Glc, dark gray; +Glc, orange; +Glc-Glc, green; +Glc+Glc, light gray. Data for **(A)** to **(F)** represent means $\pm$ SD (n = 3 to 4 biological replicates).

centers. Respiration (oxygen consumption in the dark) increased quickly upon Glc addition and remained high after Glc removal (Figure 2C), suggesting it may be governed by a different mechanism than the regulation of photosynthetic activity. The net oxygen evolution in cultures following Glc removal was lower than in photoautotrophic cultures because respiration remained high after removing Glc. Using the classical calculation of net photosynthesis (net oxygen evolution in the light minus oxygen evolution in the dark; Kirk, 2010), photosynthesis decreased from 11.1 ± 0.07 to 0.3 ± 0.07 nmol O_2 min^{-1} mm^{-3} with Glc within 84 h and then recovered to 4.9 ± 0.6 nmol O_2 min^{-1} mm^{-3} 132 h after Glc removal.

Underlying the reversible changes in photosynthesis were substantial changes to components of photosynthetic complexes. When normalized to cell volume, total chlorophyll (chlorophylls a and b) at 84 h decreased nearly 10-fold from 10.3 nmol chlorophyll mm^{-3} in photoautotrophic cells to 1.1 nmol chlorophyll mm^{-3} in heterotrophic cells (Figure 2D). However, at the same 84-h time point, the amount of total chlorophyll per cell was not significantly different between photoautotrophic and heterotrophic cultures (0.36 ± 0.04 and 0.29 ± 0.03 fmol cell^{-1}, respectively; two-tailed t test, $P = 0.056$; Figure 2E). These data suggest that chlorophyll was diluted rather than degraded as cells grew larger. After Glc removal, the amount of chlorophyll (normalized per cell or cell volume) increased substantially by the end of the Glc removal phase, although the ratio of chlorophyll a:b was relatively constant during the experiment (Supplemental Figure 1C). There was less violaxanthin and more zeaxanthin in the presence of Glc, but the total pool size of xanthophyll cycle pigments (violaxanthin, antheraxanthin, and zeaxanthin) was not significantly different between photoautotrophic and heterotrophic cultures (two-tailed t test, $P = 0.95$; Figure 2F; Supplemental Figure 1D). After Glc removal, the xanthophyll cycle pool size increased due to an increase in violaxanthin. The level of β-carotene was similar between treatments (Figure 2F; Supplemental Figure 1D).

Immunoblot analysis was used to determine changes in protein abundance of the photosynthetic apparatus (Figure 3). With Glc there was a steady decline in PSII core proteins D2 and CP43 and PSI core protein PsaA. After Glc removal, the levels of PSI and PSII proteins recovered. The large subunit cytochrome b_6 of the cytochrome $b_6 f$ (Cyt $b_6 f$) complex also declined rapidly with Glc and recovered after Glc removal. The PSI, PSII, and Cyt $b_6 f$ complexes showed a reduction and a subsequent recovery in protein content within 24 h. Furthermore, proteins in light-harvesting complexes (LHCs) of both PSI and PSII showed reversible declines with Glc. By contrast, chloroplastic and mitochondrial ATP synthase (AtpB) subunits CF$_1$β and F$_1$β, respectively, were maintained during Glc addition and removal. SDS-PAGE analysis of total protein extracts stained with Coomassie brilliant blue showed the reversible decline of the large subunit of the CO_2-fixing enzyme ribulose-1,5-bisphosphate carboxylase/oxygenase (Rubisco) at 53 kD (Supplemental Figure 1E). The changes in the protein subunits of the photosynthetic apparatus were concurrent with the changes in photosynthetic activity during the experiment.

To investigate changes in thylakoid ultrastructure, we used TEM. In photoautotrophic cells, thylakoid membranes were visible as stacked appressed membrane regions (Figure 4A). In
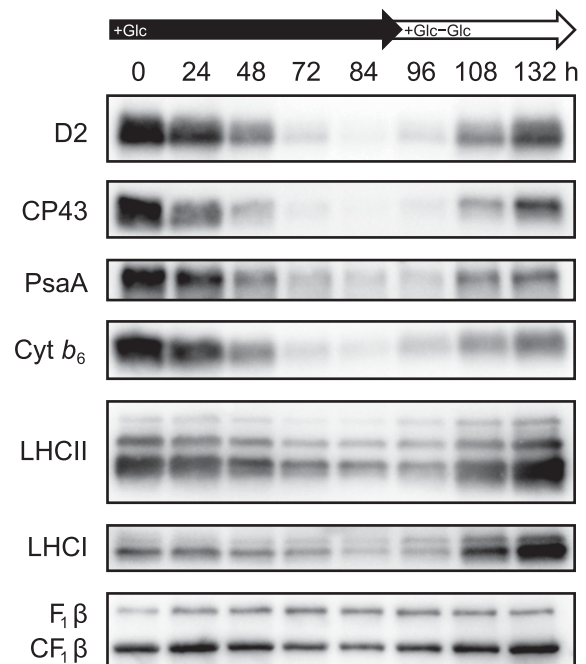
Figure 3. Glc Causes Reversible Loss of the Photosynthetic Apparatus.

Immunoblot analysis of PSII (D2, CP43), PSI (PsaA), Cyt $b_6 f$ (Cyt b_6), LHC of PSII (LHCII), LHC of PSI (LHCI), and AtpB subunits. The global anti-AtpB antibody detected both the chloroplastic and mitochondrial subunits CF$_1$β and F$_1$β (faster and slower bands, respectively; see "Methods"). Samples were normalized to total protein, and 10 μg of protein was loaded per lane. See Supplemental Figure 1E for stained total protein gel.

heterotrophic cells, there was a reduction in size and layers of these membrane regions at 84 h. To quantify these changes, we generated three-dimensional (3D) reconstructions of serial sections from TEM (Figures 4A to 4C). The overall volume of thylakoids declined nearly 14-fold, and relative thylakoid volume (as a percentage of the chloroplast) decreased from 16 to 2%. Thylakoid membranes of heterotrophic cells had a reduced number of layers in appressed membrane regions compared to photoautotrophic cells, and the mode of layers decreased from 3 to 2 (Figure 4D). Appressed membrane regions with ≥6 layers were observed only in photoautotrophic cells. Furthermore, thylakoid membranes of heterotrophic cells were shorter in length than those of photoautotrophic cells, and the mode of thylakoid membrane lengths decreased substantially from 350-400 nm to 50-100 nm, respectively (Figure 4C). Photoautotrophic cells had a broad distribution of thylakoid membrane lengths, including some ≥1 μm, and some were nearly 5-fold longer than those from glucose-treated cells. Having both shorter membranes and a reduced number of layers contributed to the diminished volume of thylakoid membranes in Glc-treated cells (Figure 4B). Live-cell imaging using super-resolution SIM revealed changes in chloroplast structure as well as a decrease in chlorophyll fluorescence (Figure 5A). These results are consistent with the Glc-induced decline in chlorophyll per cell volume (Figure 2D). During Glc removal, layers of appressed membrane regions increased, and original thylakoid structure recovered (Figures 4A and 5A). These results
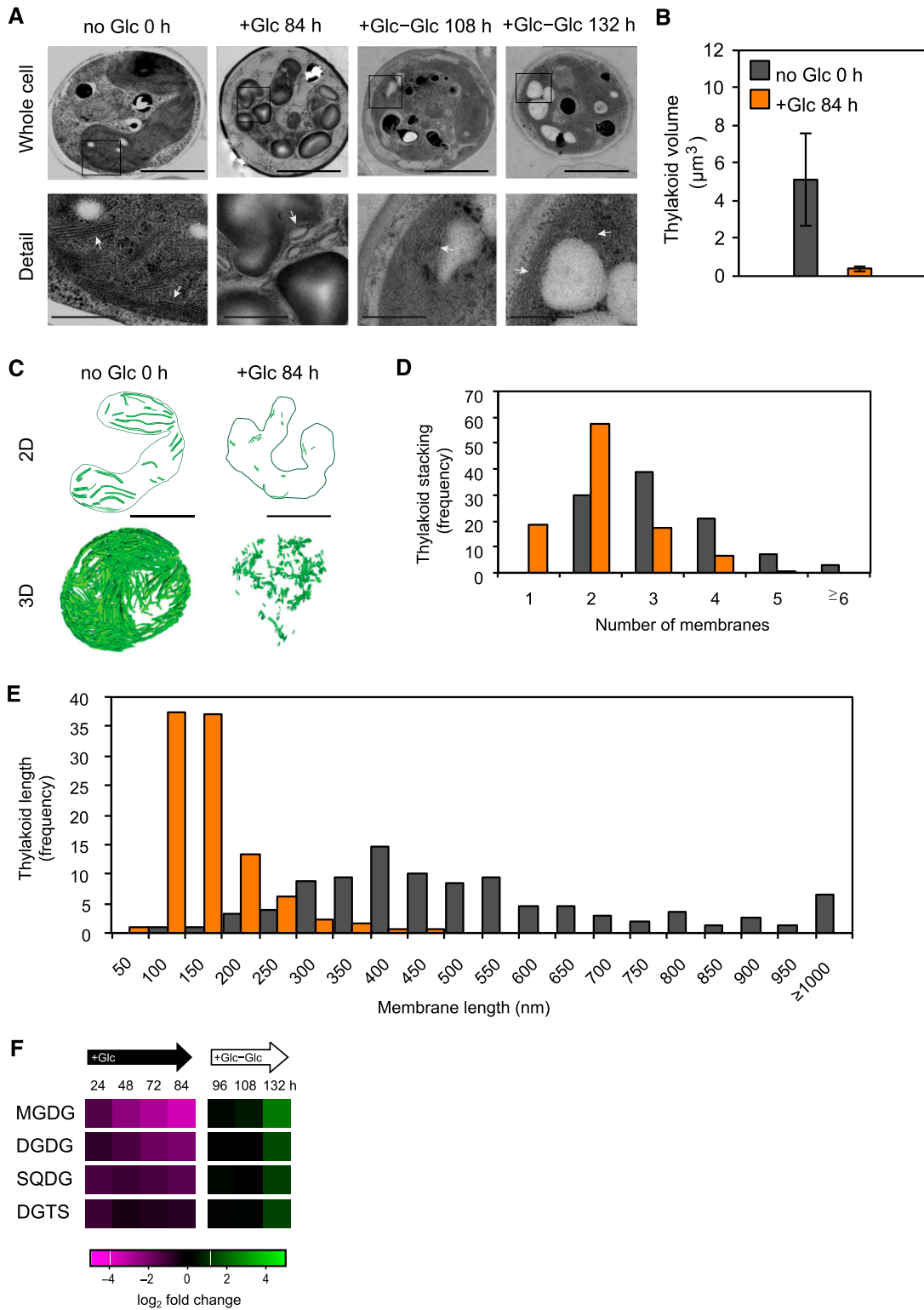
Figure 4. Thylakoid Membranes and Lipids Decrease during Glc-Induced Repression of Photosynthesis.

(A) Representative images of cell 2D TEM with thylakoid detail. White arrows point to thylakoid membranes. Whole-cell bar = 2 μm; detail bar = 0.5 μm.

(B) Thylakoid volume without and with Glc quantified by 3D reconstruction of TEM serial sections (*n* = 3 technical replicates).

(C) Cartoon of a representative 2D TEM slice of chloroplast and thylakoid membranes outlined and the 3D reconstruction of the whole cell. Bar = 2 μm.

showed that Glc has major impacts on thylakoid membrane ultrastructure.

We used liquid chromatography-tandem mass spectrometry (LC-MS/MS) to determine changes in the abundance of various lipid species. The most abundant thylakoid membrane lipids, monogalactosyldiacylglycerol (MGDG) and digalactosyldiacyl-glycerol (DGDG), declined 10-fold and 4-fold, respectively, with Glc at 84 h (Figure 4F; Supplemental Figure 2). After Glc removal, MGDG and DGDG increased fivefold and threefold, respectively, by the end of the experiment. We also observed declines and recovery in the conserved thylakoid membrane lipid sulfoquino-vosyldiacylglycerol (SQDG) and in diacylglyceryltrimethylhomoserine (DGTS), a common lipid that can be found in chloroplasts and the endoplasmic reticulum in algae (Figure 4F; Supplemental Figures 2 and 3; Thompson, 1996). MGDG, DGDG, and SQDG associate with PSII (Boudière et al., 2014), and their changes were consistent with the reversible repression and activation of photosynthesis during Glc addition and removal, respectively.

Glc Induces an Increase in Starch and Lipid Energy Stores

We used cryo-SXT and SIM to investigate changes in cellular components with Glc. Cryo-SXT and 3D reconstructions were used to quantify volumetric changes in cell organelles and storage bodies with Glc (Figures 5B and 5C; Supplemental Movies 1, 2, and 3). As cell size increased, the chloroplast increased approximately twofold in size and occupied the same percentage of the cell volume, 34 ± 4 and 33 ± 7% in photoautotrophic and heterotrophic cells, respectively. Starch granules, located within the chloroplast, increased nearly fivefold in heterotrophic cells, ultimately representing 30 ± 9% of the chloroplast volume and 10 ± 2% of the cell. Consistent with the cryo-SXT results, observations using TEM also showed an increase in starch in heterotrophic cells (Figure 4A).

One of the largest changes in Glc-treated cells was an increase in TAGs (Figure 5; Supplemental Figure 3; Supplemental Movie 2). The volume of cytoplasmic lipid bodies of heterotrophic cells increased >16-fold and reached 14 ± 3% of the volume of the cell (Figure 5C). The majority of lipid bodies were detected near the plasma membrane in heterotrophic cells but were not observed in photoautotrophic cells (Figure 5B). SIM of live cells stained for neutral lipids confirmed this result (Figure 5A). Using LC-MS/MS, we detected a >20-fold increase in TAGs in Glc-treated cells after 84 h (Figure 5D; Supplemental Figure 3). Among lipids generally, and among TAGs specifically, polyunsaturated acyl chains were depleted in Glc-treated cells, while saturated lipid species increased (Supplemental Figures 2 and 3). These results suggest that de novo FA synthesis rather than rearrangement of existing acyl chains was more likely occurring.

With both cryo-SXT and SIM, we observed a decline in the presence of lipid bodies after Glc removal (Figures 5A to 5C). Accordingly, LC-MS/MS data showed a twofold decline in TAGs (Figure 5D). Despite the increase in respiration in Glc-treated cells, the relative mitochondrial volume per cell remained similar between photoautotrophic and heterotrophic cells at 2.8 ± 1.2 and 2.2 ± 1.2%, respectively (Figure 5C). Altogether, Glc addition induced major changes in cell growth and cellular components, and these data provide evidence for a Glc-driven metabolic change resulting in increased energy stores, including starch granules and lipid bodies.

Glc Causes Reversible Global Gene Expression Changes during Regulation of Photosynthesis and Metabolism

To gain insight into genome-wide gene expression changes that initiate and coordinate the repression and activation of photosynthesis and metabolic changes during trophic transitions, we conducted an RNA sequencing (RNA-seq) experiment at the transition points of Glc addition and subsequent removal. Cultures were collected and analyzed for nuclear, plastidic, and mitochondrial gene expression at 0, 0.5, 1, 3, 6, and 12 h (n = 4 biological replicates) after Glc addition and removal in treatment and control cultures (see "Methods"). Sequences were mapped to the *C. zofingiensis* genome (v5.2.3.2; Roth et al., 2017) and assigned to each of the 15,369 gene models (Supplemental Data Set 1).

A principal component analysis (PCA) of the regularized $\log_2$-transformed counts from the resulting transcriptome profiles was plotted for both the Glc addition and Glc removal phases (Figure 6A). For Glc addition, PC1, which accounted for 59% of the variance, corresponded with the time of day, while PC2, accounting for 25% of the variance, corresponded to Glc addition. Replicate samples were tightly clustered. In contrast to Glc addition, we could not disentangle the effects of time from treatment in Glc removal. The most significant PC, representing 79% of the variance, combined both time and treatment and was observed as a rightward shift along PC1 for the Glc removal samples relative to their time-matched controls. This pattern suggests that the transcriptomic changes that are occurring in Glc removal samples also occur in heterotrophic control samples, just later in the day. The second most significant component was smaller (9% of variance) and distinguished midday time points (3 and 6 h) from early and late time points (0.5, 1, and 12 h). Taken together, our PCA demonstrates that time of day has a major effect on the transcriptomic profile of the cultures. This result is consistent with previously reported high light experiments (Roth et al., 2017). To distinguish the effects of diurnal periodicity from the effects of Glc,


Figure 4. (continued).

(D) Histogram of the number of membranes per thylakoid stack with Glc. Data represent all technical replicates (n = 3).

(E) Histogram of thylakoid length (nm) with Glc. Membrane length labels on the x-axis are the end point of the category (e.g., 50 represents the number of membranes with lengths 0 to 50 nm). Data represent all technical replicates (n = 3).

(F) Heatmap showing thylakoid membrane lipids (MGDG, DGDG, SQDG, and DGTS) plotted as $\log_2$-transformed fold change in comparisons of Glc versus photoautotrophic control and Glc removal versus heterotrophic control at each time point. Lipids are normalized to AFWD. Data represent means (n = 3 to 4 biological replicates). Supplemental Figures 2 and 3 contain abundance and fold change for each lipid species. The following color scheme is used for **(B)**, **(D)**, and **(E)**: no glc 0 h, dark gray; +glc 84 h, orange.
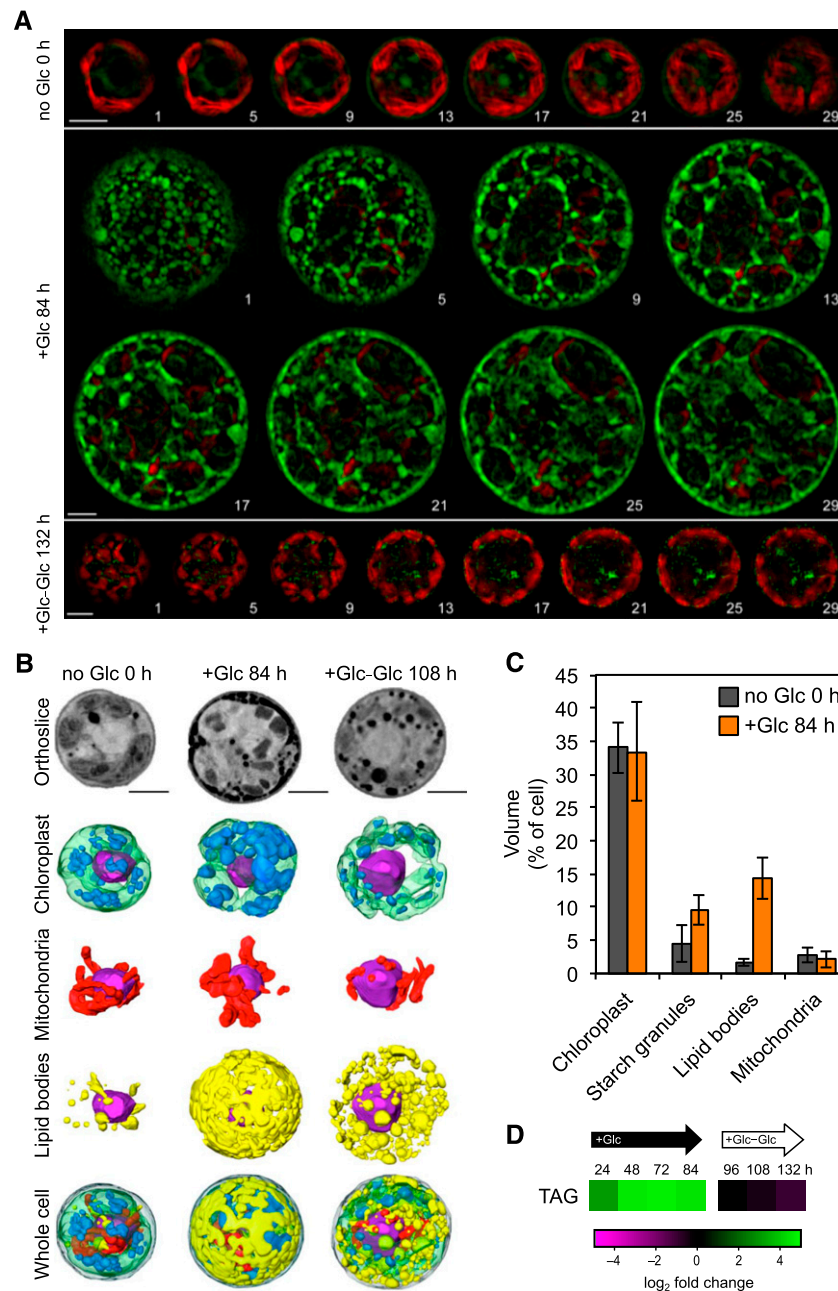
Figure 5. TAG and Starch Energy Stores Increase during Glc-Induced Metabolic Changes.

(A) Representative images of live-cell SIM showing merged chlorophyll autofluorescence (red, 650 to 730 nm) and BODIPY neutral lipid dye fluorescence (green, 505 to 550 nm). Each number corresponds to the selected focal plane of serial optical sections moving from surface of the cell to the center with a z-step of 101 nm. Bar = 2 μm.

(B) Representative cryo-SXT of cells showing orthoslices, segmented chloroplasts containing starch granules and nucleus, mitochondrial networks and nuclei, lipid bodies and nuclei, and fully segmented cells (Supplemental Movies 1, 2, and 3). Nucleus, purple; chloroplast, green; mitochondria, red; lipid bodies, yellow; starch granules within the chloroplast, blue. Bar = 2 μm.

(C) Changes in intracellular morphology with Glc as determined by cryo-SXT. Data represent means ± SD (n = 8 to 11 technical replicates).

(D) Heatmap TAG abundance plotted as $\log_2$-transformed fold change in comparisons of Glc versus photoautotrophic control and Glc removal versus heterotrophic control at each time point. Lipids are normalized to AFDW. Data represent means (n = 3 to 4 biological replicates). Supplemental Figure 3 contains abundance and fold change for each lipid species.
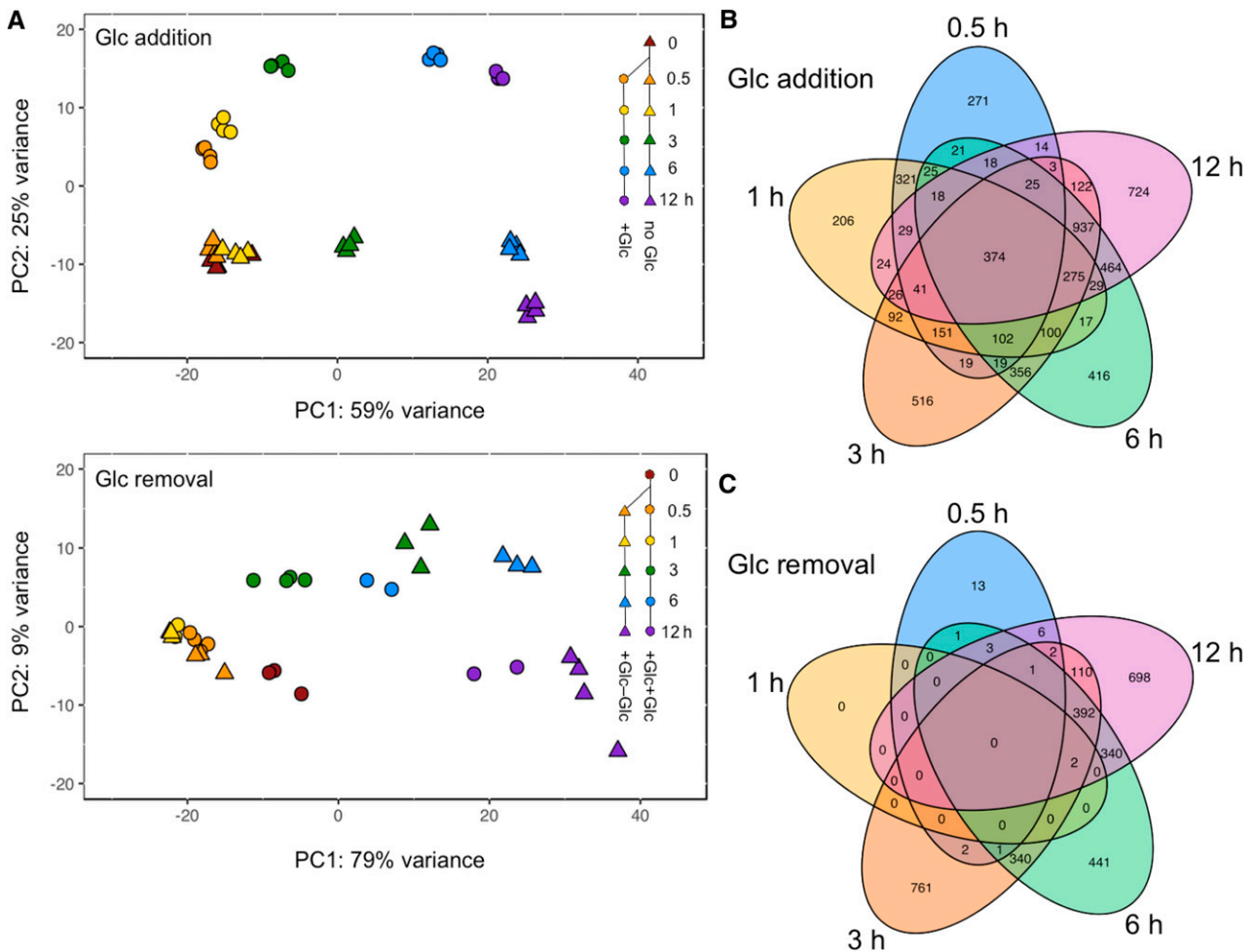
Figure 6. Transcriptome Response to Glc Addition and Removal.

RNA abundance changes during Glc addition and removal. At t = 0, Glc addition or Glc removal was initiated. Samples were collected in quadruplicate at 0, 0.5, 1, 3, 6, and 12 h for photoautotrophic and heterotrophic controls and at 0.5, 1, 3, 6, and 12 h for Glc addition and removal. Transcript abundances for each sample were determined by RNA-seq. DEGs are more than twofold up- or downregulated relative to time-matched controls with BH-adjusted P < 0.01. See also Figure 3 for DEGs during Glc addition and removal and Venn diagram showing reversible differential expression during Glc addition and removal.
(A) A PCA of regularized log_2-transformed counts for the 500 genes with the highest variance during Glc addition (top panel) and removal (bottom panel) is plotted. Supplemental Data Set 5 contains the genes used in the PCA. For Glc addition, the photoautotrophic controls (circles) and the Glc addition samples (triangles) are displayed with time points indicated by color. The two most significant components, accounting for 84% of the variation, are shown. For Glc removal, the heterotrophic control (circles) and the Glc removal samples (triangles) are displayed with time points indicated by color.
(B) Venn diagram comparing the number of DEGs at each time point (0.5, 1, 3, 6, and 12 h) for Glc addition.
(C) Venn diagram comparing the number of DEGs at each time point (0.5, 1, 3, 6, and 12 h) for Glc removal.

all analyses of the RNA-seq experiments focused on differences compared with time-matched controls.

To examine the effects of Glc addition and removal on gene expression, we identified differentially expressed genes (DEGs) between treatment and control at each time point. Genes were considered differentially expressed if they showed a greater than twofold change in transcript abundance (Benjamini–Hochberg [BH]-adjusted P < 0.01) in either direction between Glc and photoautotrophic control cultures or Glc removal and heterotrophic control cultures (Figures 6 and 7). More than a third of the genes in the transcriptome were differentially expressed in response to Glc at one or more time points in this

study (6356 of 15,369 genes, Figure 7). Consistent with the PCA, more genes were differentially expressed upon Glc addition than upon Glc removal (5755 and 3113, respectively), and the two treatments shared 2512 DEGs. There were 374 DEGs shared across all time points in Glc addition experiments (Figure 6B). By contrast, Glc removal had no DEGs shared across all time points (Figure 6C). There were two distinct stages of gene expression in Glc removal: an early stage (0.5 and 1 h), which had minimal changes (31 DEGs combined), and a mid-late stage, which had a large number of DEGs. The later time points (3, 6, and 12 h) each had >1500 DEGs and shared 395 DEGs (Figures 6 and 7). It is possible that the delayed response

was due to intercellular stores of Glc that had not yet been depleted. With Glc addition, 64% of the DEGs were downregulated, whereas the opposite was true with Glc removal, as 63% of genes were upregulated. Seventy-five percent of the DEGs that were upregulated upon Glc removal were also downregulated with Glc addition (Figure 7). Conversely, 68% of downregulated DEGs upon Glc removal were upregulated DEGs with Glc addition.
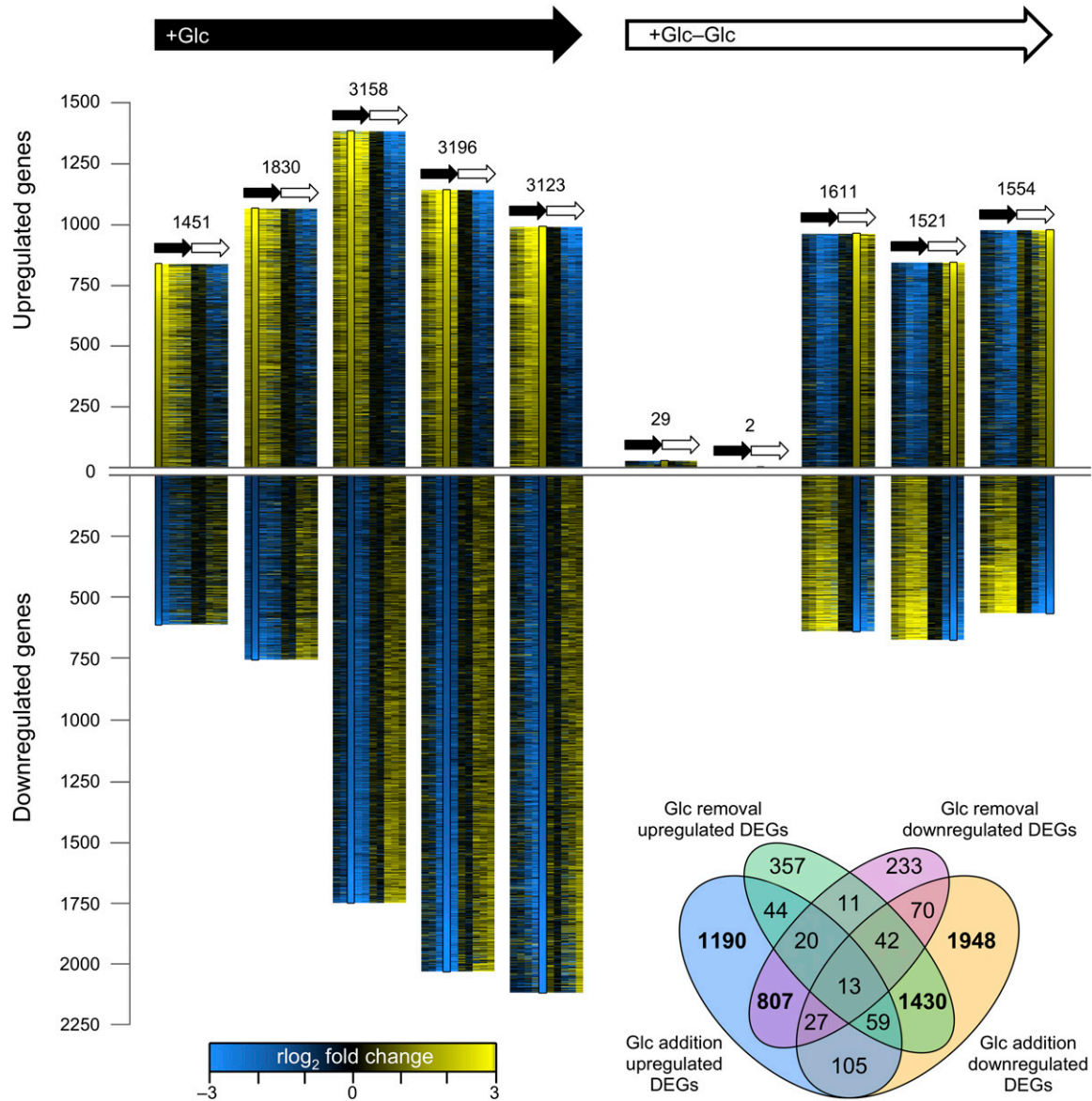
Figure 7. Genome-Wide Transcriptome Responses during Glc Addition and Removal Reveal Specific Reversible Patterns.

Gene expression changes during Glc addition and removal. Genes were considered to be DEGs if they were more than twofold up- or downregulated relative to time-matched control samples with a BH-adjusted P < 0.01. On left is plotted the number of DEGs in a comparison of Glc-treated samples versus photoautotrophic controls at each time point. On right, the same comparison was made for Glc removal samples versus heterotrophic controls. The number of DEGs is indicated by the height of the bar above the line for upregulated DEGs or below the line for downregulated DEGs, and the total is indicated above each bar. The difference between treatment and its respective control was calculated in terms of regularized (r)$\log_2$-transformed fold change of counts and plotted in the black box for each time point using the included color scale. Data represent means ($n = 2$ to 4 biological replicates). For comparison, the fold change of each DEG at all other time points in both Glc addition and removal is presented flanking the black box. The columns below the small black and white arrows indicate, from left to right, 0.5, 1, 3, 6, and 12 h after Glc addition and removal, respectively. Inset: A Venn diagram is used to demonstrate the overlap in the numbers of DEGs upregulated or downregulated during Glc addition and Glc removal. Regions with >500 DEGs are highlighted in bold.

Functional Enrichment Analysis Reveals Pathways Involved in Photosynthetic and Metabolic Changes

To gain insight into the pathways that respond after Glc addition and subsequent removal, all expressed genes (mean fragments per kb of exon per million mapped reads [FPKM] ≥1 across all time points; 13,428 total) were grouped based on their coexpression using *k*-means clustering analysis with six centers (Figure 8). Next, we used enrichment of BioCyc pathway annotations as an unbiased approach to identify key functions in each of the clusters (Supplemental Data Set 2).

Cluster 1 was characterized as highly up- and downregulated upon Glc addition and Glc removal, respectively (Figure 8). Pathways enriched in cluster 1 included glycolysis, FA and biotin biosynthesis, and acetyl-CoA generation (Supplemental Data Set 2). Cluster 1 also included genes encoding hexose phosphate isomerases, which had highly dynamic expression patterns, although their associated pathways were not enriched. Cluster 2 was characterized as moderately up- and downregulated upon Glc addition and Glc removal, respectively, and as in cluster 1, FA metabolism pathways were enriched. Furthermore, putative Suc biosynthesis, starch metabolism, and the methylerythritol phosphate pathway for isoprenoid biosynthesis were enriched. Because both starch synthesis and degradation pathways were enriched, there is potential for a futile starch cycle during Glc addition. Pathways related to the metabolism of very long chain FAs were also enriched.

In contrast to clusters 1 and 2, cluster 6 showed the opposite trend: gene expression was highly down- and upregulated upon Glc addition and Glc removal, respectively. Pathways enriched in cluster 6 included photosynthesis, chlorophyll biosynthesis, β-oxidation of FAs, and the glyoxylate cycle (Supplemental Data Set 2). Pathways enriched related to FA metabolism included catabolism and long-chain β-ketoacyl-synthase–related pathways. Lipid catabolism by peroxisome-mediated β-oxidation of FAs and the glyoxylate cycle were both upregulated during Glc removal, suggesting a mechanism for TAG breakdown and mobilization and resynthesis of Glc from acetyl-CoA.

Cluster 5 had a pattern of slight decreasing and increasing upon Glc addition and Glc removal, respectively, but no pathways were functionally enriched (Supplemental Data Set 2). Clusters 3 and 4 did not show clear trends with respect to changes in gene expression during Glc addition and removal, and only one pathway was enriched in each cluster. Mitochondrial genes were present in clusters 3 and 4, and chloroplast genes were split among clusters 3, 4, 5, and 6.

We also conducted functional enrichment analyses on four groups of DEGs: upregulated upon Glc addition, downregulated upon Glc addition, upregulated upon Glc removal, and downregulated upon Glc removal (Supplemental Data Set 2). We found a similar set of metabolic pathways enriched by this analysis as were revealed by the *k*-means cluster analysis, but this grouping allowed us to distinguish pathways that have similar initial kinetics but demonstrate divergent behavior. This approach identified additional enriched pathways related to nitrate reduction and TAG biosynthesis.

In summary, the most striking enriched pathways from both approaches in genes whose expression increased upon Glc
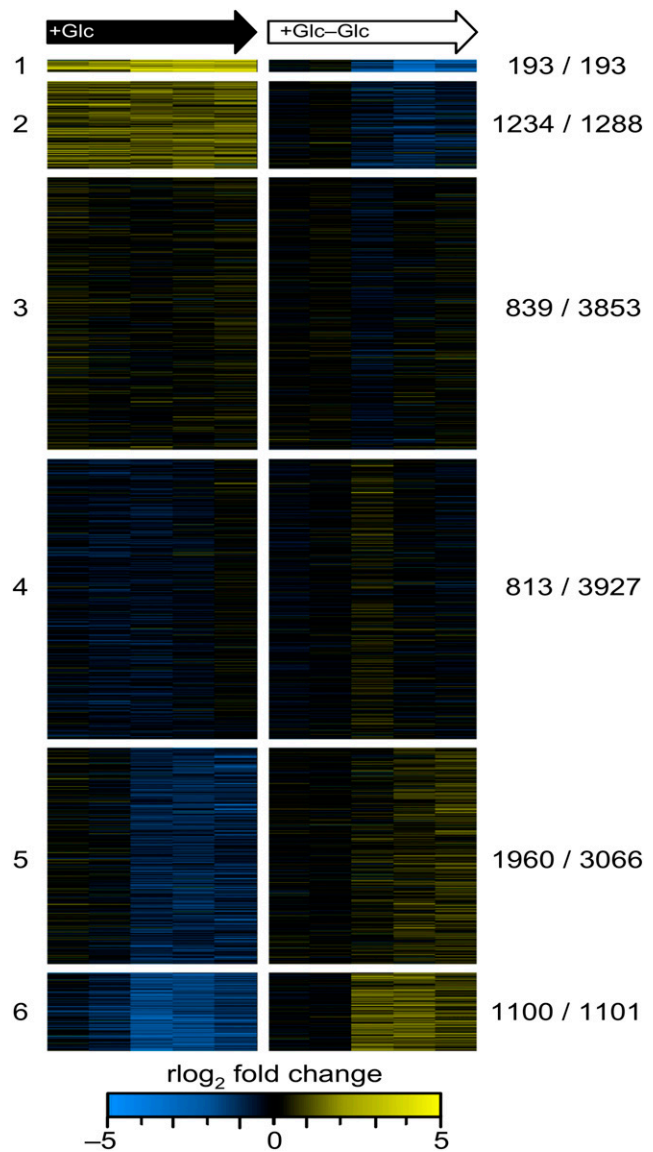
Figure 8. Heatmap of *k*-Means Clustering of Gene Coexpression Reveals Reversible Glc-Induced Patterns.

The fold changes between Glc addition versus the photoautotrophic control and between Glc removal versus the heterotrophic control were calculated for samples at 0.5, 1, 3, 6, and 12 h posttreatment for all genes with ≥1 FPKMs mean expression across all samples (13,307 of 15,369 total genes). Data represent means (*n* = 2 to 4 biological replicates). The resulting data were subjected to *k*-means clustering with six centers and plotted as a heatmap of regularized (r)log$_2$-transformed fold change for each gene in each cluster. The number of DEGs (more than twofold up- or downregulated) and the total number of genes for each cluster are indicated to the right.

addition and decreased after Glc removal were related to glycolysis, starch, and FA metabolism including TAG biosynthesis. The most notable pathways enriched in genes whose expression is decreased upon Glc addition and increased with Glc removal were those encoding enzymes of β-oxidation, the glyoxylate

cycle, and photosynthesis including chlorophyll biosynthesis and other related activities.

Reversible Glc-Induced Upregulation of Ketocarotenoid Biosynthesis Gene Expression

To further characterize expression of carotenoid biosynthesis genes, we mapped RNA abundance changes upon Glc addition and removal onto the carotenoid biosynthetic pathway (Figure 9; Supplemental Data Set 3). These data in combination with the analysis of photosynthetic pigments (Figures 1 and 2; Supplemental Figure 1D) revealed a preference for changes in expression of the β-carotene branch over the α-carotene branch of the pathway upon Glc addition: lycopene beta-cyclase (*LCYB1*) was upregulated, while lycopene epsilon-cylase (*LCYE1*) was downregulated. Beta-carotene hydroxylase (*CHYB1*) and beta-

ketolase (*BKT*)*1*, which are critical for the production of astaxanthin in *C. zofingiensis* (Li et al., 2008; Roth et al., 2017), were upregulated in Glc-treated cells, consistent with the increase in ketocarotenoids (Figures 1B and 2F; Supplemental Figure 1D). Moreover, expression of the gene encoding the chlorophycean violaxanthin de-epoxidase (CVDE1), which converts violaxanthin to zeaxanthin (Li et al., 2016), was upregulated, while zeaxanthin epoxidase (*ZEP1*), the gene responsible for the reverse reaction, was downregulated. These expression changes correlated with an increase in the proportion of zeaxanthin to violaxanthin (Figure 2F; Supplemental Figure 1D). *C. zofingiensis* also has an ortholog of plant-type *VDE1* whose transcript abundance is similar to that of *CVDE1*, but its expression was insensitive to Glc addition. Alternatively, *VDE1* was upregulated upon Glc removal, suggesting that its gene product could be utilized under distinct conditions relative to *CVDE1* or that it has another role in
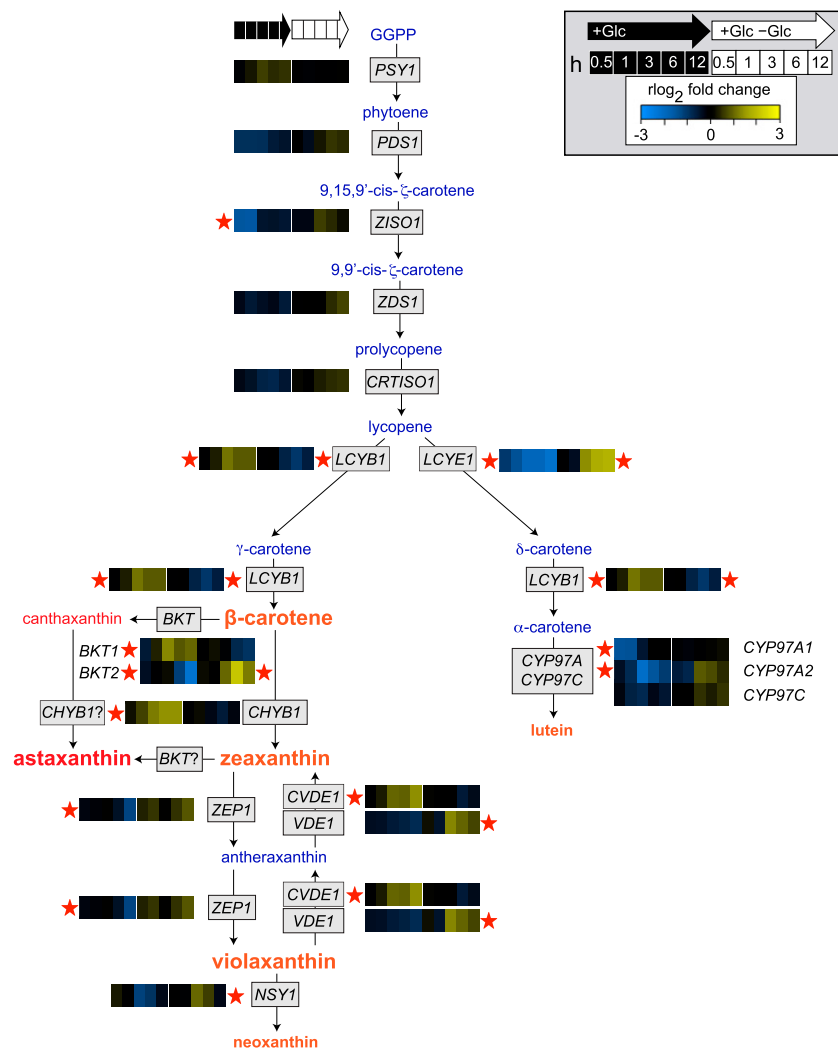
Figure 9. Glc Causes Reversible Increases in Ketocarotenoid Gene Expression.

The carotenoid pathway with regularized (r)log$_2$-transformed fold change in gene expression upon Glc addition and subsequent removal relative to time-matched control sample plotted as a heatmap. Data represent means (*n* = 2 to 4 biological replicates). DEGs are indicated by a red star (more than twofold up- or downregulated, BH-adjusted P < 0.01). Fold-change values and gene IDs are in Supplemental Data Set 3.

C. zofingiensis. Upon Glc removal, the changes in gene expression and ultimately pigment abundances were reversed (Figures 1, 2, and 9; Supplemental Figure 1D). Although these changes were modest, our results showed that Glc caused a reversible change in expression of genes associated with the production of ketocarotenoids.

Reversible Glc-Induced Downregulation of Chlorophyll Biosynthesis Genes

We mapped the dynamics of the expression of genes encoding chlorophyll biosynthesis and degradation functions upon Glc addition and subsequent removal (Figure 10; Supplemental Data Set 3). Genes involved in chlorophyll biosynthesis were differentially downregulated with Glc. This trend was observed for nearly all steps of tetrapyrrole biosynthesis, magnesium chelation, and phytol addition. Transcripts of enzymes related to chlorophyll degradation or phytol biosynthesis did not show trends toward coordinated regulation and were insensitive to Glc treatment. Chlorophyll biosynthesis genes that were differentially downregulated with Glc were generally upregulated upon Glc removal. These results demonstrate that Glc caused changes in chlorophyll biosynthesis gene expression, and these changes correspond to the observed changes in chlorophyll abundance (Figures 2D and 2E).

Reversible Glc-Induced Changes in Glycolysis and FA Biosynthesis Gene Expression

To examine metabolic changes that may lead to increased accumulation of TAGs during heterotrophy (Figure 5D; Supplemental Figure 3), we mapped RNA abundance changes onto glycolysis and FA metabolism pathways upon Glc addition and removal (Figure 11; Supplemental Data Set 3). The abundances of transcripts for most enzymes in glycolysis were increased in Glc-treated cells. RNA encoding the first step in glycolysis, *HXK1*, rapidly increased 30-fold by 0.5 h and 40-fold by 1 h after Glc addition. Upon Glc removal, the abundance of transcripts encoding glycolytic enzymes was unchanged or decreased.

Pyruvate generated from glycolysis is further oxidized to form acetyl-CoA by the pyruvate dehydrogenase (PDH) complex. After Glc addition, genes encoding the three subunits of the plastid-localized PDH complex were reversibly upregulated in response to Glc (Figure 11; Supplemental Data Set 3). The PDH components E1α, E1β, E2, and E3 (encoded by pyruvate decarboxylase [*PDC2*], pyruvate dehydrogenase [*PDH2*], dihydrolipoamide acetyltransferase [*DLA2*], and dihydrolipoamide dehydrogenase *DLD2*, respectively) were regulated in near synchrony, demonstrating a tightly regulated response.

Other genes encoding components of FA biosynthesis were also reversibly regulated by Glc (Figure 11; Supplemental Data Set 3), including those encoding acetyl-CoA carboxylase (*ACC*), acyl carrier protein (*ACP2*), malonyl-CoA:ACP transacylase (*MCT1*), subunits of the FA synthase complex (beta-ketoacyl ACP synthase [*KAS1-3*], beta-hydroxyacyl ACP dehydrase/dehydratase [*HAD1*], beta-ketoacyl ACP reductase [*KAR1*], enoyl ACP

reductase [*ENR1*]), and a fatty acid desaturase (FAD; *SAD1*). By contrast, transcript abundance of genes required for the synthesis of thylakoid lipids MGDG, DGDG, SQDG, and DGTS were relatively insensitive to Glc addition and removal. We did, however, observe dynamic regulation of plastid galactoglycerolipid degradation (*PGD1*), whose homolog is responsible for MGDG degradation in *C. reinhardtii* (Li et al., 2012). *FAT1*, encoding an enzyme responsible for the export of free FA from the chloroplast, was reversibly upregulated with Glc.

Many extra-plastidic enzymes involved in lipid biosynthesis were differentially expressed upon Glc addition and removal (Figure 11; Supplemental Data Set 3). Genes involved in TAG biosynthesis, *GPAT2*, *LPAAT2*, *PAP4*, and *DGAT*s (*DGTT3*, *DGTT6*, *DGTT7*), were reversibly upregulated with Glc. The gene encoding major lipid droplet protein (MLDP1), a protein scaffold found in lipid droplets whose abundance is correlated with cellular TAG content (Moellering and Benning, 2010), was particularly responsive during Glc addition and removal. We also identified a potential TAG lipase gene (*LIP1*) that was dynamically regulated with Glc in accordance with TAG accumulation with Glc. FADs, which determine the position and degree of saturation of lipid acyl chains, also had reversible upregulation with Glc. *FAD6B* and *FAD7B*, whose products are predicted to be chloroplast localized, had the strongest response to Glc. The reversible RNA abundance changes in TAG biosynthesis genes were consistent with observed changes in TAG abundance and the presence of cytoplasmic lipid droplets (Figure 5).

DISCUSSION

In this study, we have characterized a trophic transition in a green alga and identified biological processes involved in disassembly and assembly of photosynthesis and associated changes in heterotrophic carbon metabolism in the light. We have integrated cellular physiology studies, lipid analyses, transcriptomics, TEM, cryo-SXT, and SIM to provide a detailed characterization of the tightly controlled, reversible regulation of photosynthesis and metabolism. It is notable that the repression and activation of photosynthesis characterized in this study occurs in the light. In addition to the interesting biology of *C. zofingiensis* during its metabolic changes during trophic transitions, recent interest in this organism has grown because of its commercial potential: it can amass large amounts of TAGs in parallel with the high-value ketocarotenoid astaxanthin while accumulating biomass.

The first report of a visual color change in algae upon addition of sugars was from Krüger (Krüger, 1894) when he isolated *A. protothecoides* from tree sap and cultured it in a variety of conditions. In the 1960s and 1970s, Hase and coauthors further explored this phenomenon, and they described algal cells as "glucose-bleached" (summarized in Hase, 1975). Hase and coauthors focused on the dark degeneration and specifically the regeneration of chloroplasts in the light. Their work in *A. protothecoides* provides a good comparison with this study. However, the trebouxiophyceaen *A. protothecoides* is distinct from the chlorophyceaen *C. zofingiensis* in that it does not accumulate astaxanthin during growth on Glc.
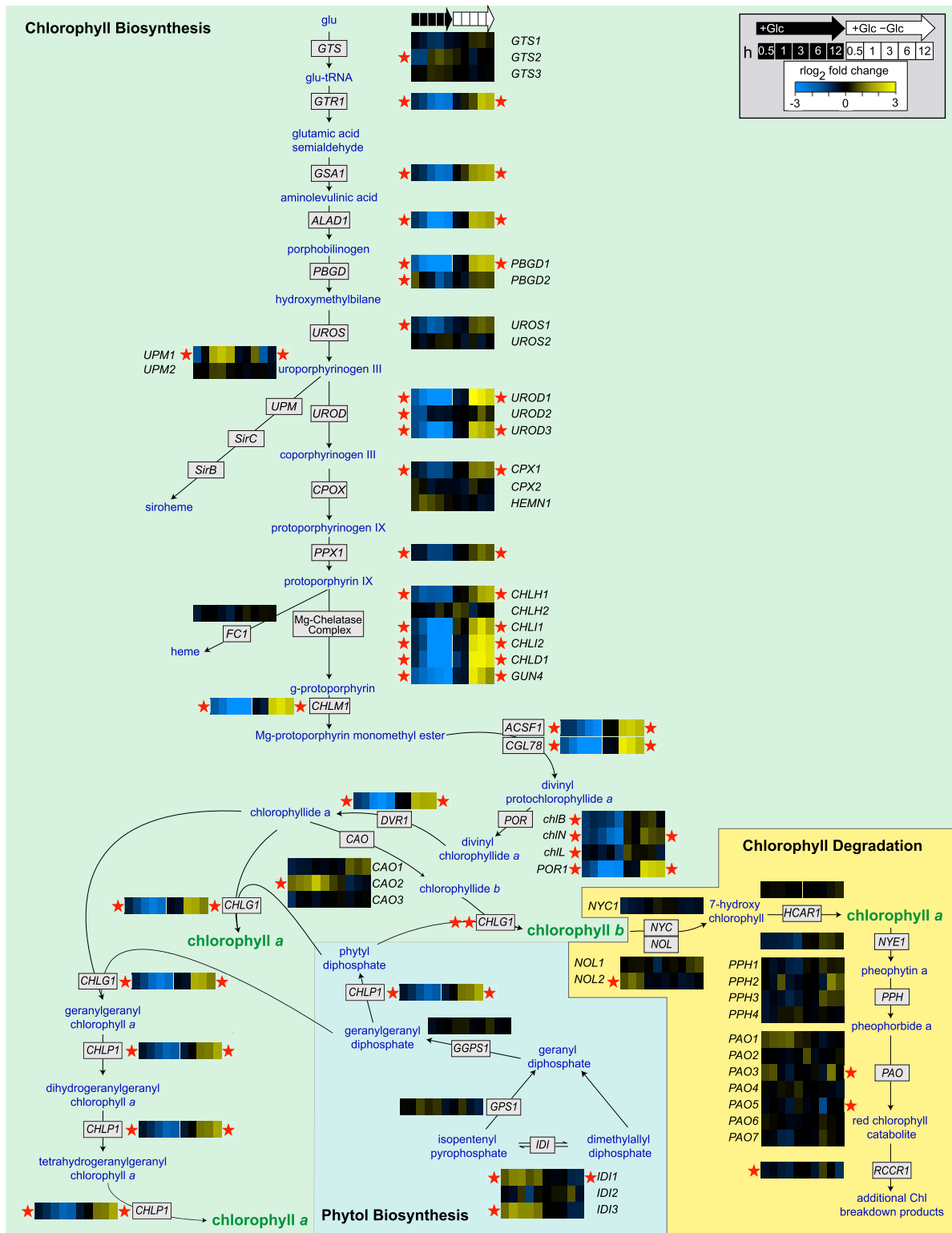
Figure 10. Glc Causes Reversible Decreases in Chlorophyll Biosynthesis Gene Expression.

The chlorophyll biosynthesis and degradation pathways with regularized (r)log$_2$-transformed fold change in gene expression upon Glc addition and subsequent removal relative to time-matched control sample plotted as a heatmap. Data represent means (n = 2 to 4 biological replicates). DEGs are indicated by a red star (more than twofold up- or downregulated, BH-adjusted P < 0.01). Fold-change values and gene IDs are in Supplemental Data Set 3.

Figure 11. Gene Expression Changes Associated with Altered Carbon Flux with Glc Indicate Increased Glycolysis and FA Biosynthesis.

Glycolysis and FA metabolism pathways with regularized (r)log$_2$-transformed fold change in gene expression upon Glc addition and subsequent removal relative to time-matched control sample plotted as a heatmap. Data represent means (n = 2 to 4 biological replicates). DEGs are indicated by a red star (more than twofold up- or downregulated, BH-adjusted P < 0.01). Fold-change values and gene IDs are in Supplemental Data Set 3.

Coordinated Assembly and Disassembly of Photosynthesis

While many algae have flexible metabolism, it is unusual to completely turn off photosynthesis during trophic transitions (Shugarman and Appleman, 1966; Semenenko, 1981). Here, we have shown that *C. zofingiensis* transitions from photoautotrophy through mixotrophy to heterotrophy with the addition of exogenous Glc in the light. Photosynthesis reversibly turns off, and the photosynthetic machinery is degraded and regenerated during these trophic shifts. Within a few days, we observed complete loss of PSII activity and cessation of oxygen evolution in the light (Figure 2). In conjunction with the absence of photosynthetic activity, the abundance of reaction center proteins of PSI and PSII decreases dramatically (Figure 3), the abundance of dominant thylakoid membrane lipids associated with PSII decreases (Figure 4F), thylakoid membranes are truncated (Figures 4D and 4E), and thylakoid volume decreases 14-fold (Figure 4B). The abundance of PSII core proteins appears to be affected more than that of PSI core proteins, and core proteins of both PSs are affected more than LHCs (Figure 3). As with *C. zofingiensis*, differential degradation of PSI and PSII was observed with Glc in *A. protothecoides* (Hase, 1975). PSI and PSII may become decoupled during the transition from photoautotrophy to heterotrophy, and residual PSI could retain some activity within the time scale of this experiment. Consistent with the changes in Rubisco abundance that we observed (Supplemental Figure 1E), declines in Rubisco activity with Glc were reported previously for *C. zofingiensis* (Zhang et al., 2017) and *A. protothecoides* (Oshio and Hase, 1972). Glc removal quickly restores photosynthetic activity and oxygen production, although respiration of cells remains high, suggesting that some physiological differences in cells remain within the time frame of this experiment. Similarly, during Glc removal, CO_2 fixation and Rubisco activity recovered quickly in *A. protothecoides*, and light was necessary to reach high rates of photosynthesis (Oh-Hama et al., 1965; Oshio and Hase, 1972). Additionally, in *A. protothecoides*, photosynthetic and CO_2 fixation enzymes are degraded under heterotrophic conditions, reflecting the changes in photosynthesis (Gao et al., 2014).

C. zofingiensis thylakoid membranes in photoautotrophic conditions showed substantial variation in both length, ranging from 70 to 2100 nm, and stacking, ranging from two to six membranes (Figure 4D). In addition to the loss of thylakoid volume as measured by serial-section TEM (Figures 4B and 4C), the degeneration of thylakoid ultrastructure with Glc was visible from the changes in chlorophyll fluorescence using SIM (Figure 5A). Degradation of thylakoid membranes was previously seen, but was not quantified in *A. protothecoides* (Shihira-Ishikawa and Hase, 1964; Oh-Hama et al., 1965). In *C. zofingiensis*, in addition to the decrease in thylakoid membranes, the chloroplast grew in proportion to the cell size with Glc. During Glc removal, light is necessary for the organization of fully developed thylakoid structure in *A. protothecoides* (Oh-Hama et al., 1965), and a carbohydrate reserve rather than photosynthesis was hypothesized to contribute to the regeneration of thylakoid membranes (Hase, 1975). Using antibiotics, it was shown that cell division is not necessary for chloroplast regeneration and the formation of chlorophyll, RNA, and protein in *A. protothecoides* (Aoki and Hase, 1965).

Changes in photosynthesis correlated with decreases in the expression of chlorophyll biosynthesis genes rather than increases in the expression of chlorophyll degradation genes (Figure 10). The amount of chlorophyll per cell remained constant during this experiment (Figure 2E). It is unknown where the remaining chlorophyll molecules are located, but it is possible that they are contained in LHCs or sequestered outside the chloroplast. LHCs are the most abundant thylakoid membrane protein and contain chlorophyll and, while the abundance of LHCs was reduced with Glc, they are still present. It may be possible for chlorophyll to be sequestered through autophagy, a process of membrane trafficking in which damaged or toxic cellular components are recycled and degraded, as was observed in *C. reinhardtii* (Pérez-Pérez et al., 2017). Future investigations into the location of the remaining chlorophyll molecules and/or what are they bound to could resolve this interesting issue. With Glc addition, the cells grew larger, and this resulted in a decrease in chlorophyll by cell volume (Figure 2D). It is likely that if the Glc phase of the experiment continued, the reduction of chlorophyll biosynthesis gene expression would have ultimately led to a decrease in chlorophyll on a per cell basis. During Glc removal, there was increased expression of chlorophyll biosynthesis genes, resulting in an increase in chlorophyll within the cells. Future research could determine whether the remaining chlorophyll was recycled or synthesized de novo during thylakoid biogenesis. Similarly, a reversible decline in chlorophyll absorbance was observed in 5 d with Glc in *A. protothecoides* (Shihira-Ishikawa and Hase, 1964). It was also noted in *Chlorella* that nutrient concentrations affected the changes in chlorophyll and chloroplast structures (Shihira-Ishikawa and Hase, 1964), and this is likely the case for *C. zofingiensis*, providing an important area for future investigations.

Previous work on *Chlorella* sp. K showed that dGlc, a Glc analog that can be transported into the cell but not metabolized, causes inhibition of photosynthesis, suppression of both chlorophyll biosynthesis and Calvin cycle enzymes, and degradation of the chloroplast ultrastructure (Semenenko, 1981; Zvereva et al., 1981). Because these studies used a Glc analog rather than Glc, these data suggest the repression of photosynthesis response is due to Glc signaling rather than Glc metabolism. Future research will elucidate whether Glc and/or a downstream metabolite is involved in the Glc-dependent effects on metabolism in algae. Our current study describes controllable repression and activation of photosynthesis that will enable future studies on mechanisms of regulation of photosynthesis and thylakoid assembly and disassembly in green algae.

Time-Resolved Transcriptomics Reveal Biological Processes Induced during Trophic Transitions

High-temporal resolution sampling during both the transition from photoautotrophy to heterotrophy and from heterotrophy to photoautotrophy allowed us to characterize in detail the changes in RNA abundance during algal metabolic rearrangement. Not surprisingly, our transcriptome results showed a strong influence of the diurnal cycle, as has been well characterized in *C. reinhardtii* (Zones et al., 2015). However, using time-matched controls, we were able to distinguish the effects of the diurnal cycle and trophic

transitions. Repressing and activating photosynthesis and transitioning to different trophic modes involved a global change including a third of all gene models. This response was considerably larger (approximately sixfold) than the transcriptomic response to high light in *C. zofingiensis* (Roth et al., 2017). Glc addition caused differential gene expression of a substantially larger number of genes than did Glc removal (5755 and 3113 DEGs, respectively). These experiments highlighted the reversibility of gene expression between the two treatments, suggesting that these are likely to be transcriptionally regulated biological processes.

The photosynthetic and metabolic changes in the cell were driven by changes in gene expression. The large-scale, reversible changes in the transcriptome correlated with the addition and removal of Glc and were consistent with significant physiological modifications. Enriched pathways in our analyses included glycolysis, starch synthesis and degradation, chlorophyll biosynthesis, FA metabolism and TAG biosynthesis, photosynthesis, β-oxidation, and the glyoxylate cycle. The increase in astaxanthin and FA biosynthesis genes with Glc is consistent with findings of a previous study (Huang et al., 2016). Similarly, sugars in plants and algae play a major role in regulating thousands of genes, and studies have shown repression of photosynthetic genes and induction of carbon storage genes (Rolland et al., 2006; Gao et al., 2014; Sheen, 2014; Fan et al., 2015). This study provides a high-resolution transcriptome analysis revealing the biological processes that underlie the reversible, Glc-mediated transitions between photoautotrophy and heterotrophy in *C. zofingiensis*. This data set and our coexpression analyses will also enable future studies to investigate other processes during trophic transitions in green algae.

Transcriptome Dynamics Correspond with Changes in Energy Reserves and Ketocarotenoids

The repression and activation of photosynthesis that we observed coincided with a redirection of carbon metabolism toward increased energy reserves in the form of starch and lipids, particularly TAGs. We observed a nearly fivefold increase in starch volume within 84 h (Figures 5B and 5C), and the starch pathway was functionally enriched in cluster 2 (Figure 8), which contained genes that were upregulated with Glc addition and downregulated with Glc removal. Surprisingly, starch degradation was also functionally enriched; therefore, the observed starch accumulation may be due to posttranscriptional mechanisms that promote the anabolism. This study, consistent with previous studies, showed that Glc could induce production of TAGs and astaxanthin in *C. zofingiensis* (Huang et al., 2016; Zhang et al., 2016). However, *C. zofingiensis* contrasts with *Chlorella pyrenoidosa*, which accumulates starch during heterotrophy but lipids during photoautotrophy (Fan et al., 2015).

Combining lipid analyses and transcriptional changes, our study provides an in-depth look at genes involved in altering lipid abundances and provides insights into mechanisms controlling TAG accumulation. We observed increases in TAGs and decreases in thylakoid membrane lipids, in particular MGDG. Transcriptome analysis showed significant increases in gene expression of nearly all genes involved in glycolysis, and this perhaps provides more pyruvate for increased lipid biosynthesis.

With Glc, multiple steps of FA biosynthesis and elongation were upregulated, similar to what was previously reported at 96 h with Glc under low light (Huang et al., 2016). In *A. protothecoides*, an increase in FAs was observed with Glc, and it was hypothesized that Glc leads to an increase in glucose-6-phosphate and ultimately acetyl-CoA, which serve as precursors for FAs and lipid biosynthesis (Matsuka et al., 1969).

RNA abundance of genes leading to production of MGDG, DGDG, SQDG, and DGTS was relatively unresponsive or downregulated during the experiment. By contrast, *PGD1* was actively upregulated with Glc (Figure 11). *PGD1* encodes a lipase whose homolog in *C. reinhardtii* degrades MGDG by removing an acyl chain that is either recycled into MGDG or exported and added to TAGs (Li et al., 2012; Du et al., 2018). Thus, our data provide evidence that the decrease in MGDG abundance results from active lipid degradation rather than decreased expression of biosynthetic enzymes and that *PGD1*-derived free FAs may be precursors to TAGs. During Glc removal, *PGD1* is downregulated, and MGDG abundance increases and TAG abundance decreases. Moreover, genes involved directly in TAG biosynthesis were upregulated with Glc. MLDP is a green algal–specific protein that was shown in *C. reinhardtii* to form a proteinaceous coat to stabilize mature TAG lipid droplets (Moellering and Benning, 2010; Tsai et al., 2015). In our study, *MLDP* was strongly upregulated with Glc and downregulated with Glc removal, providing further functional support for this protein in a different green algal species. With Glc, we also observed significant reversible downregulation of the gene encoding a potential TAG lipase (*LIP1*). The putative TAG lipase might remove a fatty acyl chain that may be transported to the peroxisome and could be recycled to acetyl-CoA via β-oxidation or ultimately to malate via the glyoxylate cycle. Our results identify this lipase as a potential bioengineering target for increasing the accumulation of TAGs in *C. zofingiensis*. Glc removal led to restoration of photosynthesis and the photosynthetic machinery within a day, and this was followed by a decrease in TAGs and an increase in thylakoid membrane lipids concomitant with changes in RNA abundance for genes involved in glycolysis, lipid biosynthesis, and FA modification (Figure 11).

We also observed an increase in ketocarotenoids with Glc, as can be seen both by the change in culture color from green to orange and by ketocarotenoid peaks in the high performance liquid chromatography (HPLC) chromatogram (Figure 1B; Supplemental Figure 1D). This result is consistent with results from multiple studies quantifying these pigments (e.g., Ip et al., 2004; Ip and Chen, 2005; Li et al., 2008; Sun et al., 2008). The upregulation of *LCYB1* and downregulation of *LCYE1* gene expression with Glc support a preference for the β-carotene branch, which produces the ketocarotenoids, similar to a previous study conducted under low light and longer timescales (Huang et al., 2016). Huang et al. (2016) reported an increase in RNA abundance of both *BKT1* and *BKT2* transcripts at 72 and 96 h, whereas our study within 12 h showed upregulation of *BKT1*. The function of *BKT2* and whether it is involved in astaxanthin biosynthesis remain unknown, as *bkt1* mutants do not make astaxanthin under high light (Roth et al., 2017). A previous study suggested that Glc induces ketocarotenoid biosynthesis genes *BKT1* and *CHYB1* through different signaling pathways but that both are necessary for astaxanthin accumulation (Li et al., 2008).

Recently, the connection between the accumulation of TAGs and astaxanthin in *C. zofingiensis* has become of interest to improve commercialization of this alga. Either Glc addition or nitrogen starvation stimulates the accumulation of TAGs and astaxanthin (this study; Breuer et al., 2012; Mulders et al., 2014; Huang et al., 2016; Zhang et al., 2016). Astaxanthin accumulates primarily as astaxanthin esters with mono- or diesterified FAs. It is possible that the esterified forms of astaxanthin colocalize with TAGs in cytoplasmic lipid droplets near the cell membrane, but further evidence is needed to test this hypothesis. It has been hypothesized that ketocarotenoid and FA biosynthesis compete for carbon precursors and reducing power (Zhang et al., 2016). In *Haematococcus pluvialis* (Chlorophyceae), there is coordination between astaxanthin and FA biosynthesis at the metabolite level, but not the transcript level (Chen et al., 2015a). Additionally, both free and esterified forms of astaxanthin are made in the endoplasmic reticulum in *H. pluvialis* (Chen et al., 2015a). In *C. zofingiensis*, it remains unknown where astaxanthin is formed and whether β-carotene or zeaxanthin is the precursor to astaxanthin.

Glc-Induced Changes in Cell Division

Proper regulation of cell growth and division not only is a critical aspect of development but also has the potential to be exploited to improve production of microalgae. Not surprisingly, in this study we observed a sixfold increase in biomass of *C. zofingiensis* cultures with Glc and light compared with photoautotrophic cultures within 84 h (Figure 1C). The increased culture biomass is primarily due to increasing cell size rather than cell division. Heterotrophic cell density increased slowly (Figure 1D), but cells reach greater than sevenfold the volume of photoautotrophic cells (Figure 1E). These data suggest that cells with Glc invest in growing larger rather than in cell division, at least initially. Although *C. zofingiensis* can mature into cells with multiple nuclei (Fucikova and Lewis, 2012), our study was conducted with young cells that contain a single nucleus and chloroplast. By contrast, Glc removal promoted cell division, resulting in smaller cells. Thus, our study shows that Glc is able to affect cell cycle regulation and control cell division, albeit through unknown mechanisms. Like *C. reinhardtii*, *C. zofingiensis* exhibits multiple fission (Dönz, 1934; Roth et al., 2017), in which a cell undergoes multiple rounds of rapid cell division to produce 2^n daughter cells (Umen, 2018). Multiple fission in *C. zofingiensis* results in similar-sized daughter cells regardless of whether they came from photoautotrophic or heterotrophic cells. Similarly, in *A. protothecoides*, Glc delays DNA synthesis and cell division (Hase, 1975). Future studies with *C. zofingiensis* should provide insight into nutritional influences on cell growth and division.

C. zofingiensis Is an Emerging Model Organism

C. zofingiensis is emerging as a new model for oleaginous algae. With a small genome of only ~58 Mbp (Roth et al., 2017) and a readily controlled photosynthetic and metabolic switch, as shown by this study, *C. zofingiensis* can be exploited as an experimental organism for investigating Glc responses, carbon metabolism and partitioning, disassembly and reassembly of the photosynthetic apparatus, astaxanthin biosynthesis, as well as TAG accumulation and remobilization from cytoplasmic oil bodies. Ultimately, understanding these fundamental processes in *C. zofingiensis* will enable bioengineering approaches to enhance production of biofuel precursors and high-value products from microalgae.

METHODS

Culture Strain and Growth

We used the *Chromochloris zofingiensis* strain SAG 211-14 obtained from the Culture Collection of Algae (Göettingen University), whose genome was published recently (Roth et al., 2017). The cells were grown in liquid cultures shaking at 100 to 150 rpm under diurnal conditions (16-h-light/8-h-dark cycle) at a light intensity of 100 μmol photons m^{-2} s^{-1} (cool white spectrum) at 25°C, as previously described (Roth et al., 2017). Cells were grown in Proteose medium (UTEX Culture Collection of Algae, University of Texas, Austin) with Chu's micronutrient solution (2 mL/L; UTEX Culture Collection of Algae). For experiments, cells were grown in large, liquid, photoautotrophic preculture until cells reached exponential growth (~4×10^6 cells/mL). The cells were mixed and distributed into separate beakers the day prior to the experimental start time. Unless otherwise specified, cells were collected by centrifugation (at 3000 to 20,000*g*, for 2 to 10 min). Three to four biological replicates were used, and parallel samples started at the same time were used at the different time points. Cells were counted and sized with the Multisizer 3 Coulter counter (Beckman Coulter).

Two-Phase Glc Addition and Removal Experiment

Cells were grown as described above and distributed into 66 separate beakers. For the first phase of the experiment (0 to 84 h), Glc was added to photoautotrophic cultures in the light. To maintain Glc-replete conditions, 10 mM Glc was added every 24 h. Photoautotrophic cultures were maintained as no-Glc controls. Samples were collected at 0, 24, 48, 72, and 84 h. For the second phase of the experiment (84 to 132 h), Glc was removed from heterotrophic cultures in the light. After 84 h of Glc, heterotrophic cells were collected by centrifugation, the supernatant was discarded, and cells were resuspended in fresh medium without Glc. Heterotrophic cultures were also collected by centrifugation, the supernatant was discarded, and cells were resuspended in fresh medium with Glc as heterotrophic controls. Subsequently, 10 mM Glc was added every 24 h to heterotrophic controls. Samples were collected at 96, 108, and 132 h from the beginning of the experiment. For the Glc addition RNA-seq analysis, the liquid preculture of photoautotrophically grown cells was distributed into 44 separate beakers 1 d before the start of the experiment: enough for four biological replicates of each time point and condition. Samples were collected at 0.5, 1, 3, 6, and 12 h after Glc addition to photoautotrophic cultures and at 0, 0.5, 1, 3, 6, and 12 h in photoautotrophic controls. For Glc removal, the liquid preculture of photoautotrophically grown cells was distributed into 44 separate beakers 1 d before Glc was added, and cultures grew with Glc for 72 h. Samples were then collected from four biological replicate cultures at 0.5, 1, 3, 6, and 12 h after Glc removal from heterotrophic cultures and 0, 0.5, 1, 3, 6, and 12 h in heterotrophic controls. Glc was added or removed ~3 h after the start of the light phase (8:00 AM), and all samples were collected during the light phase.

Measurement of Photosynthetic Efficiency

Photosynthetic efficiency was measured with the FMS2 system (Hansatech Instruments) as previously described (Roth et al., 2017), with

modifications. After cells were dark acclimated while shaking for 30 min, 3.5×10^6 cells were collected onto a glass fiber filter that was then placed into the instrument's leaf clip. The maximum efficiency of PSII, $(F_m - F_o)/F_m = F_v/F_m$, was measured using a 0.5-s saturating pulse (at >2000 μmol photons $m^{-2} s^{-1}$).

Measurement of Oxygen Consumption and Net Oxygen Evolution

Oxygen consumption and net oxygen evolution were measured with the Oxygraph Plus System (Hansatech Instruments) as previously described (Peers et al., 2009), with modifications. Cell densities were adjusted to 10^7 cells/mL and dark acclimated for >30 min. Oxygen consumption was measured over 1 min after reaching steady state in the dark at a constant temperature of 25°C. Net oxygen evolution was also measured over 1 min after reaching steady state under actinic light of 100 μmol photons $m^{-2} s^{-1}$ at a constant temperature of 25°C. For cultures with cell volumes larger than 100 $μm^3$, additional samples with a cell density of $\leq 5 \times 10^6$ cells/mL were used in order to achieve an OD_{750} of ~0.2 to 0.4. Oxygen consumption and net oxygen evolution were normalized to cell volume and chlorophyll.

Identification of Photosynthetic Pigments

Photosynthetic pigments were identified by HPLC (1100 HPLC; Agilent) as previously described (Roth et al., 2017). Cells were pelleted and homogenized with acetone and lysing matrix D (MP Biomedical) for 3×60 s at 6.5 m s^{-1} with the FastPrep-24 5G High Speed homogenizer (MP Biomedical). Cell debris was pelleted by centrifugation (at $20,000g$, for 3 min), and the supernatant was collected. To ensure complete extraction, acetone extractions were repeated twice. Pigments were normalized to total chlorophyll per cell and to cell volume because the cell volume changed during the experiment.

Immunoblot Analysis

Cells were pelleted by centrifugation and homogenized in solubilization buffer (Tris-HCl, pH 6.8, 3.5% w/v SDS, 6% w/v urea, and 10% w/v glycerol) and lysing matrix D for 3×60 s with a FastPrep-24 5G High Speed homogenizer (at 6.5 m s^{-1}; MP Biomedical). Chloroform:methanol protein purification was performed as previously described (Wessel and Flügge, 1984). Proteins were resolubilized in solubilization buffer containing 25 mM DTT. For analysis, 10 μg of protein was run with loading buffer on Any kD Mini-PROTEAN TGX gels (Bio-Rad), transferred to polyvinylidene difluoride membranes, and immunoblotted with anti-PsbD (1:5000; Agrisera), anti-PsbC (1:1000; Agrisera), anti-PsaA (1:1000; Agrisera), anti-PetB (1:10,000; Agrisera), anti-P17 (1:5000; Bassi and Wollman, 1991), anti-Lhca2 (1:5000; Agrisera), or anti-AtpB (1:5000; Agrisera) antibodies. Because the AtpB antibody detects both chloroplast and mitochondrial $F_1\beta$ subunits, Expasy compute was used to discriminate between these two variants. CzCPg01090 was predicted to be ~50 kD and Cz03g32200 was predicted to be ~65 kD. Additionally, both PredAlgo and TargetP prediction software predicted an N-terminal mitochondrial targeting sequence for Cz03g32200. Proteins were visualized with an anti-rabbit IgG antibody (1:10,000; GE Healthcare) and ChemiDoc MP imaging system (Bio-Rad). Protein concentration was determined using the DC protein assay (Bio-Rad), and equal protein levels were confirmed by Coomassie Brilliant Blue R 250 staining. Two biological replicates for each primary antibody were used. Supplemental Table 1 includes catalog information for antibodies.

Transmission Electron Microscopy

Cells were concentrated by centrifugation, loaded into 100-μm-deep specimen carriers, and ultrarapidly frozen using a Bal-Tec HPM 010 high-pressure freezer without a filler. Specimen carriers containing the samples were transferred onto the surface of the frozen freeze-substitution medium (1% OsO_4 and 0.1% uranyl acetate) and placed inside an EM AFS2 freeze substitution processor (Leica) equilibrated to −90°C using the following protocol: 38 h at −90°C, 32.5-h linear warm up to −25°C, 12 h at −25°C followed by a 5-h linear warm up to 0°C. After three to four quick acetone rinses over 5 to 10 min, the samples were removed from the carriers and cut into smaller pieces if needed. The samples were introduced to a graduated Epon Araldite resin series (6.2 g of Eponate 12, 4.4 g of Araldite 502, 12.2 g of dodecenyl succinic anhydride, and 0.8 mL of benzyl-dimethyl amine [BDMA; only added for the final 100% changes]) of 25, 50, and 75% resin:acetone. The following infiltration protocol was used: 25% for 1 h, 50% for 2 h, 75% for 4 h, 1×10 min rinse with 100% resin, 100% overnight, $2 \times$ 10 min 100% + BDMA, followed by a final 4 h with 100% + BDMA. After infiltration, the samples were transferred to PELCO flat embedding molds and polymerized for 2 d at 60°C. Sections were cut 70 nm thick on a Reichert-Jung Ultracut E ultramicrotome, picked up on Formvar-coated slot grids, and poststained for 7 min in 2% aqueous uranyl acetate and 4 min in Reynold's lead citrate. Sections were examined and imaged on a FEI Tecnai 12 transmission electron microscope operated at 120 kV, and images were acquired on a Gatan 2Kx2K Ultrascan 1000 digital camera. Approximately six to eight technical replicates were used for 2D electron micrographs, and three technical replicates were used for 3D reconstructions. Electron micrographs of serial sections were recorded using Serial EM software package (Digital Micrograph 1.80.58 for GMS 1.8.0). To process the images, electron micrographs of serial sections were aligned using the 3dmod 4.7.12 software package. Segmentation and 3D reconstructions of cell organelles and internal membranes were performed using Amira (v5.3.3) manual segmentation tools. The histogram of thylakoid membrane length was binned as 0 to 50 nm, 51 to 100 nm, and so on and labeled as 50 to represent the number of membranes with lengths 0 to 50 nm.

Cryo-Soft X-Ray Tomography

SXT of cryopreserved *C. zofingiensis* was done as previously described (Le Gros et al., 2012, 2014). Briefly, cells were pelleted by centrifugation and loaded into custom-made, thin-walled glass capillaries that were previously dipped in a solution of 100-nm gold nanoparticles and subsequently used as fiducial markers for alignment of the x-ray projections. Capillaries with cells were cryopreserved by plunging the tip into an ~90K reservoir of liquid propane at 2 m s^{-1} using a custom-made fast-freezing apparatus. Soft x-ray tomographic data were acquired using the cryogenic soft x-ray microscope in the National Center for X-ray Tomography at the Advanced Light Source in Berkeley, California, as previously described (Roth et al., 2017). Projection images were collected at 517 eV using a Fresnel zone plate with a resolution of ~50 nm as the objective lens. For each data set, 90 projection images were acquired spanning a range of 180°. During data acquisition, the specimen was kept in a stream of helium gas that had been cooled to liquid nitrogen temperatures to maintain cryopreservation of the sample. Depending on the thickness of the specimen, exposure times for each projection image varied between 200 and 350 ms. 3D reconstructions of the x-ray projections were calculated using the software package IMOD (v4.7.12) after manually tracking fiducial markers on adjacent images for alignment. AMIRA (v5.3.3) was used on technical replicates ($n = 8$ to 11) to semiautomatically segment the 3D volumetric reconstructions into subcellular compartments (lipid droplets, chloroplasts, starch, and mitochondria) based on their different gray-level ranges. Segmentation of the nucleus was performed manually.

Structured Illumination Microscopy

To stain neutral lipids, the pelleted cells were resuspended with 5 μg/mL BODIPY 493/503 dye (Thermo Fisher Scientific) in Proteose medium as

previously described (Iwai et al., 2018). The cells were incubated in the dark for 10 min and washed (three times) with 1 mL of Proteose medium and centrifuged (at 3000g, for 1 min). After washing, the pelleted cells were resuspended with 50 to 200 μL of 0.5% low-melting-point agarose prepared with Proteose medium, and then 4 μL of resuspended cells was immediately mounted between two microscope cover slips. After the agarose solidified, the mounted cover slips were placed in the Attofluor cell chamber (Thermo Fisher Scientific). *C. zofingiensis* live cells (technical replicates $n \geq 8$) were observed using a Zeiss Elyra PS.1 structured illumination microscope with objective lens Plan-APOCHROMAT 100×/1.46 (Zeiss). Chlorophyll and BODIPY were excited by 642 and 488 nm lasers, respectively, and fluorescence from each fluorophore was acquired through 650 to 730 nm and 505 to 550 nm band-pass filters, respectively. The image acquisition was done as fully controlled by ZEN software (v2012 SP5; Zeiss). Raw images were processed to reconstruct super-resolution 3D images using ZEN software.

Ash-Free Dry Weight

To measure the total amount of organic material, ash-free dry weight (AFDW) was determined. Pellets were transferred to preweighed aluminum pans and then weighed after drying at 80°C for 2 d and after combusting in an oven at 450°C for 4 h. The difference in pellet weight between these two drying conditions was used to calculate the AFDW (Schagerl and Müller, 2006).

Lipid Extraction

For lipid extraction, LC-MS grade solvents were obtained from Sigma-Aldrich and HPLC grade chloroform from VWR. Prior to lipid extraction, cell pellets were lyophilized to dryness (FreeZone 2.5 Plus; Labconco) and powdered by bead beating with a 3.2-mm stainless steel bead in a bead-beater (Mini-Beadbeater-96; BioSpec Products) for 5 s (three times). To extract lipids, a chloroform-based lipid extraction was performed using a modified Bligh–Dyer approach (Bligh and Dyer, 1959). Water (60 μL) was added to the powdered pellet, vortexed, and 600 μL of 2:1 methanol:CH$_3$Cl (final ratio of 2:1:0.8 MeOH:CH$_3$Cl:H$_2$O) was added; this was followed by brief vortexing and incubating for 15 min in a sonic water bath (Scientific Aquasonic Water Bath model 150HT; VWR). An additional 200 μL of CH$_3$Cl and 300 μL of water were added (final ratio of 1:1:0.9 MeOH:CH$_3$Cl:H$_2$O), followed by brief vortexing and incubating for 10 min in the sonic water bath. Samples were centrifuged (at 2655g, for 2 min), and 200 μL of the bottom lipid-enriched chloroform phase was transferred to a new tube. An additional 200 μL of chloroform was added, followed by another round of sonication and centrifugation, and the bottom chloroform phase was combined with the previously collected extract. Chloroform extracts were dried in a SpeedVac (SPD111V; Thermo Fisher Scientific) and stored at −20°C.

Lipid Analysis

LC-MS/MS was performed on lipid extracts. Extracted lipids were resuspended in 3:3:4 isopropanol:acetonitrile:methanol (IPA:ACN:methanol), with the resuspension volume varied for each sample to normalize by AFDW and the resuspension solvent containing a 4 μM internal standard mixture of deuterium-labeled lipids (1-hexadecanoyl-2-(9Z-octadecenoyl)-sn-glycero-3-phospho-(1'-rac-glycerol-1',1',2',3',3'-d5), 1,2-dipalmitoyl-sn-glycero-3-O-4'-[N,N,N-trimethyl(d9)]-homoserine, oleic acid, 1-palmitoyl-d31-2-oleoyl-sn-glycero-3-[phospho-L-serine], 1-palmitoyl-d31-2-oleoyl-sn-glycero-3-phosphate, 1-palmitoyl-d31-2-oleoyl-sn-glycero-3-phosphoethanolamine, 1-palmitoyl-d31-2-oleoyl-sn-glycero-3-phosphocholine, 1,3-di-(9Z-hexadecenoyl)-2-hydroxy-sn- glycerol-d5, 1,3(d5)-diheptadecenoyl-2-(10Z-heptadecenoyl)-glycerol; Avanti Polar Lipids, Inc.; Supplemental Table 1). Ultra HPLC (UHPLC) reverse phase chromatography was performed using

an Agilent 1290 LC stack, with MS and MS/MS data collected using a Q Exactive Orbitrap MS (Thermo Fisher Scientific). Full MS spectra were collected from m/z 80 to 1200 at 70,000 resolution in both positive and negative modes, with MS/MS fragmentation data acquired using stepped 10-, 20-, and 30-eV collision energies at 17,500 resolution. Chromatography was performed using a C18 column (ZORBAX Eclipse Plus C18, Rapid Resolution HD, 2.1 × 50 mm, 1.8 μm; Agilent) at a flow rate of 0.4 mL/min with a 2-μL injection volume. Samples were analyzed using a gradient on the C18 column (55°C) that was first equilibrated with 80% buffer A (40:60 water:acetonitrile with 5 mM ammonium acetate and 0.1% formic acid) for 1.5 min, buffer A reduced to 45% with buffer B (90:10 IPA:ACN with 5 mM ammonium acetate and 0.1% formic acid) over 2.5 min, then to 20% A over 6 min where it was held for isocratic elution for 2 min, then reduced to 0% A over 1.5 min, and finishing with isocratic elution in 100% buffer B for 3.5 min. Samples consisted of four biological replicates each and four extraction controls, with sample injection order randomized and an injection blank (2 μL of 3:3:4 IPA:ACN:methanol) run between each sample.

Lipid Identification and Analyses

Exact mass and retention time coupled with MS/MS fragmentation spectra were used to identify lipids. For a detected compound, its lipid class was determined based on characteristic fragment ions or neutral loss, coupled with exact mass to determine specific lipid identity (number of carbons in FA tails and degree of unsaturation) (Murphy, 2015). XCalibur software (Thermo Fisher Scientific) was used to visualize raw data, and MetAtlas, a custom software created in-house, was used to extract peak heights and corresponding MS/MS spectra of detected lipids from the raw data. In positive mode, DGTS lipids ionized as [M+H]$^+$ with a characteristic fragment ion, m/z 236.1; MGDG and DGDG lipids as [M+NH$_4$]$^+$ with a neutral loss of 179 D and 341 D, respectively; and TAGs as [M+NH4]$^+$ with FA tails detected in the MS/MS spectra. In negative mode, SQDG ionized as [M−H]$^-$ with a characteristic fragment ion, m/z 225.01. Lipid standards were run separately for analysis of MGDG, DGDG, and SQDG lipids, and deuterated internal standards DGTS and TAG were used to verify fragmentation pattern and elution times of each lipid class. Supplemental Table 1 includes catalog numbers of standards. MS results of identified lipids are summarized in Supplemental Data Set 4. Distribution frequencies of each lipid class (e.g., MGDG 34:1) were calculated for each time point. Those with a distribution of less than 0.005 D, (0.5%) at all time points, were excluded from analysis. Lipids were normalized to AFDW.

RNA Preparation and Quality Assessment

Total RNA was extracted from *C. zofingiensis* as previously described (Roth et al., 2017; Gallaher and Roth, 2018). Cells were collected by centrifugation (at 3200g, for 5 min at 4°C) during daytime, frozen in liquid nitrogen, washed with cold (-20°C) ethanol on dry ice, and ethanol was removed by centrifugation (at 2200g, for 3 min at 4°C). To break the cells open, they were homogenized with lysing matrix D on dry ice for 2 × 60 s with the FastPrep-24 homogenizer (6.0 m s^{-1}; MP Biomedicals). Lysis buffer (50 mM Tris-HCl, pH 8.0, 200 mM NaCl, 20 mM EDTA, 2% SDS, and 1 mg/mL Proteinase K) was added, samples were vortexed and incubated for 3 min at room temperature, and cell debris was pelleted by centrifugation (at 20,000g, for 3 min). One milliliter of sample was added to 10 mL of TRIzol in a MaXtract high-density tube and incubated for 3 min at room temperature. To extract RNA, 1/5 volume of chloroform was added, samples were vigorously shaken, incubated for 5 min at room temperature, and phases were separated by centrifugation (at 800g, for 5 min at 22°C) and decanting. Total RNA was precipitated by adding cold ethanol on the aqueous phase and purified using the miRNeasy mini kit (Qiagen). RNA was eluted with diethylpyrocarbonate-treated water and cleaned using an ethanol precipitation step (100% ethanol and 85 mM sodium acetate, pH 8.0),

centrifugation (at ~15,000*g*, for 5 min at 4°C), and ethanol washing. The pellet was briefly air-dried and resuspended in diethylpyrocarbonate-treated water. RNA concentration and integrity were assessed using a NanoDrop 2000 spectrophotometer (Thermo Fisher Scientific) and Agilent 2100 bioanalyzer (RNA-seq samples).

RNA-Seq Analysis

RNA-seq analysis was performed as described previously (Roth et al., 2017; Gallaher and Roth, 2018), with some modifications. In brief, RNA was depleted of rRNA by means of the RiboZero rRNA Removal Kit for plant leaves (Illumina). The remaining RNA was used as input for RNA-seq library preparation by means of the KAPA stranded RNA-seq kit (KAPA Biosystems). Libraries were sequenced with 50-nucleotide single-end reads on a HiSeq 2500 sequencer (Illumina).

Adaptor sequence was trimmed from the resulting sequencing reads by means of scythe (v0.981), and 3′ base calls with Phread scores < 30 were trimmed with sickle (v1.210). The trimmed reads were then aligned to the *C. zofingiensis* reference genome (v.5.2.3.2) available from Phytozome (http://phytozome.net) by means of RNA-STAR (v2.4.0j). Default settings were used except for –alignIntronMax 5000. Aligned reads were then assigned to *C. zofingiensis* gene models with the featureCounts program of the Rsubread package (v1.12.6) within the R statistical computing platform (v3.4.4). The following settings were used: countMultiMappingReads=TRUE, fraction=TRUE, ignoreDup=FALSE, strandSpecific=2, useMetaFeatures=TRUE, fracOverlap=0.5. Adjusted counts per gene, DEGs, and regularized log_2-transformed read counts were calculated using the DESeq2 package (v1.18.1) in R.

During the analysis, a number of samples were determined to be outliers due to problems that occurred during the library construction. Contaminating DNA in RNA-seq libraries was identified by a high percentage of intergenic reads and reads on the noncoding strand. This was quantified with Rsubread featureCounts. Overamplification of the libraries was identified as a high percentage of nuclear read duplicates, which were calculated using Picard tools MarkDuplicates (v1.138). Samples with more than 50% reads aligned intergenically, or with more than 1 SD above the mean of nuclear read duplicates were excluded from further analysis. Collectively, these filters excluded 11 of 88 samples.

In the course of this analysis, we identified an ~40-kb region of chromosome 3 (approximately chr03:1,425,408-1,465,327) that appears to be erroneously duplicated on chromosome 9 (approximately chr09:2,290,532-2,339,298) in the current genome assembly (v5.2.3.2). This duplication would suggest that Cz09g23020 and Cz03g14080 should instead be a single gene located on chromosome 3. Because both loci are identical, the RNA-seq reads that had aligned to these regions mapped equally well to either locus. To address this, we masked the duplicated portion of chromosome 9 and excluded it from the analysis.

Expression estimates in terms of FPKMs were calculated in R. PCAs of the regularized log_2-transformed counts for the 500 genes (Supplemental Data Set 5) with the highest variance were performed using the prcomp feature in R and plotted with ggplot2 (v2.2.1). Heatmaps were generated in R with the ggplot2. *k*-means clustering was performed in R with the amap package (v0.8-14). BioCyc pathway annotations were downloaded from Phytozome's BioMart (https://phytozome.jgi.doe.gov/biomart). Functional enrichments of BioCyc pathways were calculated in R using the hypergeometric distribution with BH multiple testing correction and a false discovery rate of 0.05. Venn diagrams were produced in R with the VennDiagram package (v1.6.20).

Functional annotations for pathway analysis in Figures 9, 10, and 11 were performed manually based on relatedness to annotated proteins from Arabidopsis (*Arabidopsis thaliana*) and *Chlamydomonas reinhardtii*, unless noted otherwise in Supplemental Data Set 3. When possible, gene/protein symbols were chosen based on orthology to named *C. reinhardtii* proteins.

In cases of gene duplication or ambiguous orthology, making one-to-one correspondence difficult, the root of the protein symbol from *C. reinhardtii* was used and homologs were numbered. Some exceptions apply and are noted in Supplemental Data Set 3. To highlight chloroplastic processes in Figure 11, lipid biosynthesis and FA modification exclude predicted mitochondrial isoforms. When appropriate, transit peptide predictions from PredAlgo (for details, see Roth et al., 2017) were used to assess localization (Supplemental Data Set 3).

Data Availability and Accession Number

The raw metabolomics data will be made available at the Joint Genome Institute Genome Portal (https://genome.jgi.doe.gov/portal/). The raw sequencing data and analyzed RNA-seq results are available at the National Center for Biotechnology Information (https://www.ncbi.nlm.nih.gov/) Gene Expression Omnibus archive (https://www.ncbi.nlm.nih.gov/geo/) and can be accessed using the accession number GSE92519.

Supplemental Data

Supplemental Figure 1. Glucose induces reversible repression and activation of photosynthesis.

Supplemental Figure 2. Changes in MGDG, DGDG, and DGTS lipid species during glucose addition and removal.

Supplemental Figure 3. Changes in SQDG and TAG lipid species during glucose addition and removal.

Supplemental Table 1. Additional Information on antibodies, chemicals, software, and special equipment.

Supplemental Data Set 1. Master data set of transcript abundance estimates by RNA-seq.

Supplemental Data Set 2. Functional enrichment of BioCyc metabolic pathways and enzymes within clusters of differentially expressed genes.

Supplemental Data Set 3. Differential expression of genes in selected metabolic pathways in Figures 9, 10, and 11.

Supplemental Data Set 4. Mass spectrometry and identification of lipids.

Supplemental Data Set 5. Data set of 500 genes used in principal component analysis (PCA) of glucose addition and glucose removal.

Supplemental Movie 1. Cryo-soft x-ray tomography (cryo-SXT) of photoautotrophic control.

Supplemental Movie 2. Cryo-soft x-ray tomography (cryo-SXT) of glucose addition.

Supplemental Movie 3. Cryo-soft x-ray tomography (cryo-SXT) of glucose removal.

AUTHOR CONTRIBUTIONS

M.S.R. and K.K.N. conceived the study. M.S.R., S.D.G., and K.K.N. designed experiments. M.S.R., S.D.G., D.J.W., M.I., K.B.L., M.M., A.W., N.N.A., J.S., and J.-H.C. performed the research. M.S.R., S.D.G., D.J.W., M.I., K.B.L., M.M., A.W., F.F., B.P.B., C.E.B.-H., S.S.M., and K.K.N. analyzed data. M.S.R., C.E.B.-H., C.L., M.A., T.R.N., S.S.M., and K.K.N. provided resources and/or supervision. M.S.R. wrote the article with input from all authors.

REFERENCES

Aoki, S., and Hase, E. (1965). De- and re-generation of chloroplasts in the cells of *Chlorella protothecoides*: III. Effects of mitomycin C on the process of greening and division of "glucose-bleached" algal cells. Plant Cell Physiol. **6:** 347–354.

Bassi, R., and Wollman, F.-A. (1991). The chlorophyll-a/b proteins of photosystem II in *Chlamydomonas reinhardtii*: Isolation, characterization and immunological cross-reactivity to higher-plant polypeptides. Planta **183:** 423–433.

Bligh, E.G., and Dyer, W.J. (1959). A rapid method of total lipid extraction and purification. Can. J. Biochem. Physiol. **37:** 911–917.

Boudière, L., Michaud, M., Petroutsos, D., Rébeillé, F., Falconet, D., Bastien, O., Roy, S., Finazzi, G., Rolland, N., Jouhet, J., Block, M.A., and Maréchal, E. (2014). Glycerolipids in photosynthesis: Composition, synthesis and trafficking. Biochim. Biophys. Acta **1837:** 470–480.

Breuer, G., Lamers, P.P., Martens, D.E., Draaisma, R.B., and Wijffels, R.H. (2012). The impact of nitrogen starvation on the dynamics of triacylglycerol accumulation in nine microalgae strains. Bioresour. Technol. **124:** 217–226.

Chen, G., Wang, B., Han, D., Sommerfeld, M., Lu, Y., Chen, F., and Hu, Q. (2015a). Molecular mechanisms of the coordination between astaxanthin and fatty acid biosynthesis in *Haematococcus pluvialis* (Chlorophyceae). Plant J. **81:** 95–107.

Chen, T., Liu, J., Guo, B., Ma, X., Sun, P., Liu, B., and Chen, F. (2015b). Light attenuates lipid accumulation while enhancing cell proliferation and starch synthesis in the glucose-fed oleaginous microalga *Chlorella zofingiensis.* Sci. Rep. **5:** 14936.

Dönz, O.C. (1934). *Chlorella zofingiensis*, eine neue Bodenalge. Ber. Schweiz. Bot. Ges. **43:** 127–123.

Du, Z.Y., Lucker, B.F., Zienkiewicz, K., Miller, T.E., Zienkiewicz, A., Sears, B.B., Kramer, D.M., and Benning, C. (2018). Galactoglycerolipid lipase PGD1 is involved in thylakoid membrane remodeling in response to adverse environmental conditions in *Chlamydomonas*. Plant Cell **30:** 447–465.

Fan, J., et al. (2015). Genomic foundation of starch-to-lipid switch in oleaginous *Chlorella* spp. Plant Physiol. **169:** 2444–2461.

Fucikova, K., and Lewis, L.A. (2012). Intersection of *Chlorella, Muriella* and *Bracteacoccus*: Resurrecting the genus *Chromochloris* KOL et CHODAT (Chlorophyceae, Chlorophyta). Fottea **12:** 83–93.

Gallaher, S.D., and Roth, M.S. (2018). RNA purification from the unicellular green alga, *Chromochloris zofingiensis.* Bio Protoc. **8:** e2793.

Gao, C., Wang, Y., Shen, Y., Yan, D., He, X., Dai, J., and Wu, Q. (2014). Oil accumulation mechanisms of the oleaginous microalga *Chlorella protothecoides* revealed through its genome, transcriptomes, and proteomes. BMC Genomics **15:** 582.

Harris, E.H. (2009). The Chlamydomonas Sourcebook. (Amsterdam: Academic Press, Elsevier).

Hase, E. (1975). Recent progress in the physiology of *Chlorella*. In Advance of Phycology in Japan, J. Tokida and and H. Hirose, eds (The Hague: Springer Netherlands).

Huang, W., Ye, J., Zhang, J., Lin, Y., He, M., and Huang, J. (2016). Transcriptome analysis of *Chlorella zofingiensis* to identify genes and their expressions involved in astaxanthin and triacylglycerol biosynthesis. Algal Res. **17:** 236–243.

Huss, V.A.R., Frank, C., Hartmann, E.C., Hirmer, M., Kloboucek, A., Seidel, B.M., Wenzeler, P., and Kessler, E. (1999). Biochemical taxonomy and molecular phylogeny of the genus *Chlorella* sensu lato (Chlorophyta). J. Phycol. **35:** 587–598.

Hussein, G., Sankawa, U., Goto, H., Matsumoto, K., and Watanabe, H. (2006). Astaxanthin, a carotenoid with potential in human health and nutrition. J. Nat. Prod. **69:** 443–449.

Ip, P.-F., and Chen, F. (2005). Production of astaxanthin by the green microalga *Chlorella zofingiensis* in the dark. Process Biochem. **40:** 733–738.

Ip, P.-F., Wong, K.H., and Chen, F. (2004). Enhanced production of astaxanthin by the green microalga *Chlorella zofingiensis* in mixotrophic culture. Process Biochem. **39:** 1761–1766.

Iwai, M., Roth, M.S., and Niyogi, K.K. (2018). Subdiffraction-resolution live-cell imaging for visualizing thylakoid membranes. Plant J. **96:** 233–243.

Kirk, J.T.O. (2010). Light and Photosynthesis in Aquatic Ecosystems, (New York: Cambridge University Press).

Krüger, W. (1894). Beiträge zur Kenntniss der Organismen des Saftflusses (sog. Schleimflusses) der Laubbäume. Beiträge z Morph u Physiol. Nied. Org. Leipzig. **4:** 69–116.

Le Gros, M.A., Knoechel, C.G., Uchida, M., Parkinson, D.Y., McDermott, G., and Larabell, C.A. (2012). Visualizing sub-cellular organization using soft X-ray tomography. In Comprehensive Biophysics, E.H. Egelman, ed (Oxford: Academic Press), pp. 90–110.

Le Gros, M.A., McDermott, G., Cinquin, B.P., Smith, E.A., Do, M., Chao, W.L., Naulleau, P.P., and Larabell, C.A. (2014). Biological soft X-ray tomography on beamline 2.1 at the advanced light source. J. Synchrotron Radiat. **21:** 1370–1377.

Li, X., Moellering, E.R., Liu, B., Johnny, C., Fedewa, M., Sears, B.B., Kuo, M.-H., and Benning, C. (2012). A galactoglycerolipid lipase is required for triacylglycerol accumulation and survival following

nitrogen deprivation in *Chlamydomonas reinhardtii.* Plant Cell **24:** 4670–4686.

Li, Y., Huang, J., Sandmann, G., and Chen, F. (2008). Glucose sensing and the mitochondrial alternative pathway are involved in the regulation of astaxanthin biosynthesis in the dark-grown *Chlorella zofingiensis* (Chlorophyceae). Planta **228:** 735–743.

Li, Z., Peers, G., Dent, R.M., Bai, Y., Yang, S.Y., Apel, W., Leonelli, L., and Niyogi, K.K. (2016). Evolution of an atypical de-epoxidase for photoprotection in the green lineage. Nat. Plants **2:** 16140–16140.

Liu, J., Sun, Z., Gerken, H., Liu, Z., Jiang, Y., and Chen, F. (2014). *Chlorella zofingiensis* as an alternative microalgal producer of astaxanthin: Biology and industrial potential. Mar. Drugs **12:** 3487–3515.

Matsuka, M., Miyachi, S., and Hase, E. (1969). Further studies on the metabolism of glucose in the process of "glucose-bleaching" of *Chlorella protothecoides.* Plant Cell Physiol. **10:** 513–526.

Merchant, S.S., et al. (2007). The *Chlamydomonas* genome reveals the evolution of key animal and plant functions. Science **318:** 245–250.

Moellering, E.R., and Benning, C. (2010). RNA interference silencing of a major lipid droplet protein affects lipid droplet size in *Chlamydomonas reinhardtii.* Eukaryot. Cell **9:** 97–106.

Mulders, K.J.M., Janssen, J.H., Martens, D.E., Wijffels, R.H., and Lamers, P.P. (2014). Effect of biomass concentration on secondary carotenoids and triacylglycerol (TAG) accumulation in nitrogen-depleted *Chlorella zofingiensis.* Algal Res. **6:** 8–16.

Murphy, R.C. (2015). Tandem Mass Spectrometry of Lipids: Molecular Analysis of Complex Lipids. (Cambridge: The Royal Society of Chemistry).

Oh-Hama, T., Shihira-Ishikawa, I., and Hase, E. (1965). Development of photosynthetic activities during the process of chloroplast formation in *Chlorella protothecoides.* Plant Cell Physiol. **6:** 743–759.

Oshio, Y., and Hase, E. (1972). Changes in ribulose 1,5-diphosphate carboxylase level during processes of degeneration and regeneration of chloroplasts in *Chlorella protothecoides.* Plant Cell Physiol. **13:** 955–963.

Peers, G., Truong, T.B., Ostendorf, E., Busch, A., Elrad, D., Grossman, A.R., Hippler, M., and Niyogi, K.K. (2009). An ancient light-harvesting protein is critical for the regulation of algal photosynthesis. Nature **462:** 518–521.

Pérez-Pérez, M.E., Couso, I., Heredia-Martínez, L.G., and Crespo, J.L. (2017). Monitoring autophagy in the model green microalga *Chlamydomonas reinhardtii.* Cells **6:** 36.

Rolland, F., Baena-Gonzalez, E., and Sheen, J. (2006). Sugar sensing and signaling in plants: Conserved and novel mechanisms. Annu. Rev. Plant Biol. **57:** 675–709.

Roth, M.S., Cokus, S.J., Gallaher, S.D., Walter, A., Lopez, D., Erickson, E., Endelman, B., Westcott, D., Larabell, C.A., Merchant, S.S., Pellegrini, M., and Niyogi, K.K. (2017). Chromosome-level genome assembly and transcriptome of the green alga *Chromochloris zofingiensis* illuminates astaxanthin production. Proc. Natl. Acad. Sci. USA **114:** E4296–E4305.

Schagerl, M., and Müller, B. (2006). Acclimation of chlorophyll a and carotenoid levels to different irradiances in four freshwater cyanobacteria. J. Plant Physiol. **163:** 709–716.

Semenenko, V. (1981). Metabolite regulation of chloroplast genome expression and the activity of photosynthetic apparatus. In Proceeding of the 5th International Congress on Photosynthesis, G. Akoyunoglou, ed., pp. 767–776.

Sheen, J. (2014). Master regulators in plant glucose signaling networks. J. Plant Biol. **57:** 67–79.

Shihira, I., and Krauss, R.W. (1963). *Chlorella*: Physiology and Taxonomy of Forty-One Isolates. (Baltimore, MD: Port City Press).

Shihira-Ishikawa, I., and Hase, E. (1964). Nutritional control of cell pigmentation in *Chlorella protothecoides* with special reference to the degradation of chloroplast induced by glucose. Plant Cell Physiol. **5:** 227–240.

Shugarman, P.M., and Appleman, D. (1966). Chlorophyll synthesis in *Chlorella*. II. Effect of glucose and light intensity on the lag. Plant Physiol. **41:** 1701–1708.

Sun, N., Wang, Y., Li, Y.-T., Huang, J.-C., and Chen, F. (2008). Sugar-based growth, astaxanthin accumulation and carotenogenic transcription of heterotrophic *Chlorella zofingiensis* (Chlorophyta). Process Biochem. **43:** 1288–1292.

Suzuki, S., Yamaguchi, H., Nakajima, N., and Kawachi, M. (2018). *Raphidocelis subcapitata* (=*Pseudokirchneriella subcapitata*) provides an insight into genome evolution and environmental adaptations in the Sphaeropleales. Sci. Rep. **8:** 8058.

Thompson, G.A., Jr. (1996). Lipids and membrane function in green algae. Biochim. Biophys. Acta **1302:** 17–45.

Tsai, C.H., Zienkiewicz, K., Amstutz, C.L., Brink, B.G., Warakanont, J., Roston, R., and Benning, C. (2015). Dynamics of protein and polar lipid recruitment during lipid droplet assembly in *Chlamydomonas reinhardtii.* Plant J. **83:** 650–660.

Umen, J.G. (2018). Sizing up the cell cycle: Systems and quantitative approaches in Chlamydomonas. Curr. Opin. Plant Biol. **46:** 96–103.

Wessel, D., and Flügge, U.I. (1984). A method for the quantitative recovery of protein in dilute solution in the presence of detergents and lipids. Anal. Biochem. **138:** 141–143.

Yuan, J.-P., Peng, J., Yin, K., and Wang, J.-H. (2011). Potential health-promoting effects of astaxanthin: A high-value carotenoid mostly from microalgae. Mol. Nutr. Food Res. **55:** 150–165.

Zhang, Z., Sun, D., Mao, X., Liu, J., and Chen, F. (2016). The crosstalk between astaxanthin, fatty acids and reactive oxygen species in heterotrophic *Chlorella zofingiensis.* Algal Res. **19:** 178–183.

Zhang, Z., Sun, D., Wu, T., Li, Y., Lee, Y., Liu, J., and Chen, F. (2017). The synergistic energy and carbon metabolism under mixotrophic cultivation reveals the coordination between photosynthesis and aerobic respiration in *Chlorella zofingiensis.* Algal Res. **25:** 109–116.

Zones, J.M., Blaby, I.K., Merchant, S.S., and Umen, J.G. (2015). High-resolution profiling of a synchronized diurnal transcriptome from *Chlamydomonas reinhardtii* reveals continuous cell and metabolic differentiation. Plant Cell **27:** 2743–2769.

Zvereva, M.G., Klimova, L.A., and Semenenko, V.E. (1981). Repression of RNA synthesis and breakdown in activity of chloroplast photochemical systems under the influence of 2-deoxy-D-glucose and hypertrophic accumulation of assimilates in *Chlorella* cells. Soviet Plant Physiol **27:** 1218–1228 (Engl Transl Fiziol Rast).

Regulation of Oxygenic Photosynthesis during Trophic Transitions in the Green Alga
Chromochloris zofingiensis

Melissa S. Roth, Sean D. Gallaher, Daniel J. Westcott, Masakazu Iwai, Katherine B. Louie, Maria Mueller, Andreas Walter, Fatima Foflonker, Benjamin P. Bowen, Nassim N. Ataii, Junha Song, Jian-Hua Chen, Crysten E. Blaby-Haas, Carolyn Larabell, Manfred Auer, Trent R. Northen, Sabeeha S. Merchant and Krishna K. Niyogi

This information is current as of April 16, 2019

Supplemental Data	/content/suppl/2019/02/20/tpc.18.00742.DC1.html
Permissions	https://www.copyright.com/ccc/openurl.do?sid=pd_hw1532298X&issn=1532298X&WT.mc_id=pd_hw1532298X
eTOCs	Sign up for eTOCs at: http://www.plantcell.org/cgi/alerts/ctmain
CiteTrack Alerts	Sign up for CiteTrack Alerts at: http://www.plantcell.org/cgi/alerts/ctmain
Subscription Information	Subscription Information for *The Plant Cell* and *Plant Physiology* is available at: http://www.aspb.org/publications/subscriptions.cfm